Grain Engineering of Sb_2S_3 Thin Films to Enable Efficient Planar Solar Cells with High Open-Circuit Voltage

Xinnian Liu, Zhiyuan Cai, Lei Wan, Peng Xiao, Bo Che, Junjie Yang, Haihong Niu, Huan Wang, Jun Zhu, Yi-Teng Huang, Huimin Zhu, Szymon J. Zelewski, Tao Chen,* Robert L. Z. Hoye,* and Ru Zhou*

Sb_2S_3 is a promising environmentally friendly semiconductor for high performance solar cells. But, like many other polycrystalline materials, Sb_2S_3 is limited by nonradiative recombination and carrier scattering by grain boundaries (GBs). This work shows how the GB density in Sb_2S_3 films can be significantly reduced from 1068 ± 40 to 327 ± 23 nm μm^{-2} by incorporating an appropriate amount of Ce^{3+} into the precursor solution for Sb_2S_3 deposition. Through extensive characterization of structural, morphological, and optoelectronic properties, complemented with computations, it is revealed that a critical factor is the formation of an ultrathin Ce_2S_3 layer at the CdS/Sb_2S_3 interface, which can reduce the interfacial energy and increase the adhesion work between Sb_2S_3 and the substrate to encourage heterogeneous nucleation of Sb_2S_3, as well as promote lateral grain growth. Through reductions in nonradiative recombination at GBs and/or the CdS/Sb_2S_3 heterointerface, as well as improved charge-carrier transport properties at the heterojunction, this work achieves high performance Sb_2S_3 solar cells with a power conversion efficiency reaching 7.66%. An impressive open-circuit voltage (V_{OC}) of 796 mV is achieved, which is the highest reported thus far for Sb_2S_3 solar cells. This work provides a strategy to simultaneously regulate the nucleation and growth of Sb_2S_3 absorber films for enhanced device performance.

1. Introduction

Antimony chalcogenides have emerged as promising light-harvesting materials for next-generation photovoltaic devices in recent years.[1] This V-VI system, mainly including Sb_2S_3, Sb_2Se_3, and $Sb_2(S,Se)_3$, has drawn increasing attention owing to its highly desirable features and properties, such as its composition of earth-abundant and environmentally benign elements, high thermal and environmental stability, simple binary composition, high visible light absorption coefficients (10^4–10^5 cm^{-1}), and tunable bandgaps ranging from 1.10 to 1.70 eV.[1b,c,2] Following many efforts by a growing community of researchers working on these systems, the record power conversion efficiencies (PCEs) of Sb_2S_3, Sb_2Se_3, and $Sb_2(S,Se)_3$ solar cells have reached 8.00%, 10.57%, and 10.75%, respectively.[1a,d,3] Particularly, Sb_2S_3 has a bandgap of ≈ 1.70 eV, which is the optimal value for top-cells in monolithic tandem photovoltaics with silicon

X. Liu, L. Wan, H. Niu, H. Wang, R. Zhou
School of Electrical Engineering and Automation
Hefei University of Technology
Hefei 230009, P. R. China
E-mail: zhouru@hfut.edu.cn

Z. Cai, P. Xiao, B. Che, J. Yang, T. Chen
Hefei National Research Center for Physical Sciences at the Microscale
School of Chemistry and Materials Science
University of Science and Technology of China
Hefei 230026, Anhui, P. R. China
E-mail: tchenmse@ustc.edu.cn

J. Zhu
Academy of OptoElectric Technology
Hefei University of Technology
Hefei 230009, P. R. China

Y.-T. Huang, H. Zhu, R. L. Z. Hoye, R. Zhou
Inorganic Chemistry Laboratory
Department of Chemistry
University of Oxford
South Parks Road, Oxford OX1 3QR, UK
E-mail: rlzh2@cam.ac.uk

H. Zhu
Gallium Oxide Optoelectronic Devices
Department of Physics
University of Strathclyde
Glasgow G4 0NG, UK

S. J. Zelewski
Cavendish Laboratory
University of Cambridge
JJ Thomson Ave, Cambridge CB3 0HE, UK

**ADVANCED
SCIENCE NEWS**

www.advancedsciencenews.com

**ADVANCED
MATERIALS**

www.advmat.de

bottom cells, as well as for indoor photovoltaics.[4] The low melting points ($\approx$500 °C) and high vapor pressures enable the low-temperature fabrication of flexible and lightweight devices for powering Internet of Things devices.[4b,5] According to the detailed balance limit for single p-n junctions, the maximum photovoltaic performance parameters of absorbers with a 1.70 eV bandgap are an open-circuit voltage (V_{OC}) of 1.402 V, a short-circuit current density (J_{SC}) of 22.46 mA cm^{-2}, a fill factor (FF) of 91%, and a PCE of 28.64%, under 1-sun AM 1.5G illumination.[5] However, although great performance improvements have been achieved recently, the record PCE of 8.00% for Sb_2S_3 solar cells still lags far behind its radiative efficiency limit.[1a] The primary reason behind the poor efficiency is the low V_{OC}, which has stagnated to around 550–750 mV over the past decade. This represents a V_{OC} deficit (defined as $E_g/q - V_{OC}$, E_g, and q are the bandgap and the elementary charge, respectively) of >0.9 V, which exceeds those found in other solar absorbers with similar bandgaps, such as $CH_3NH_3PbI_3$, GaAs, CdTe, etc.[5,6] Therefore, it is imperative to realize effective strategies to overcome the V_{OC} bottleneck of Sb_2S_3 solar cells.

The large V_{OC} deficit in Sb_2S_3 solar cells is generally attributed to the traps states in devices, which can occur at surfaces, in the bulk or at interfaces.[6b] First-principles calculations and experimental results have demonstrated that although Sb_2S_3 is only a binary compound, the absorber film suffers from a complex defect chemistry, mainly from sulfur vacancies (V_S), antimony vacancies (V_{Sb}), Sb antisites (Sb_S), and S antisites (S_{Sb}).[7] These point defects, especially those with deep levels, could act as recombination centers, which would lower the quasi-Fermi level splitting and further decrease the V_{OC}. Another plausible explanation for the high V_{OC} deficit, proposed by Yang et al., is that it is due to the self-trapping of photoexcited charge-carriers, setting an upper limit in the maximum V_{OC} (to approximately 0.80 V) and PCE (to approximately 16.00%) for Sb_2S_3 solar cells.[8] However, by investigating the electron-lattice interaction and theoretical limits of carrier mobility using first-principles and Boltzmann transport calculations, Wang et al. demonstrated band-like transport in Sb_2S_3 and concluded that the key limiting factor is defect-trapping rather than self-trapping.[9] This suggests that the low photovoltage of Sb_2S_3 solar cells could be surmountable with improved processing conditions to engineer the defect and interfacial properties of devices. This calls for further experimental efforts to mitigate the deleterious role of defects in Sb_2S_3.

For polycrystalline thin film-based optoelectronic devices, grain boundaries (GBs) significantly influence the optoelectronic properties of the semiconductor, and ultimately the device performance.[10] This is because GBs, where dangling or wrong bonds proliferate, would impede charge-carrier transport and increase the rate of nonradiative recombination. It has been widely suggested that Sb_2S_3 has a quasi-1D crystal structure with $[Sb_4S_6]_n$ units bonded covalently together in the c-axis direction to form $[Sb_4S_6]_n$ ribbons.[11] Although this quasi-1D structure is suggested to enable nearly benign GBs in [001]-oriented grains, the Sb_2S_3-based devices would also inevitably involve the negative effects of GBs at the terminals of ribbons in polycrystalline films.[5] It is therefore critical to minimize the GB density in Sb_2S_3 thin films to reduce nonradiative recombination losses.[12] Large, compact crystalline grains are also desirable to promote charge-carrier transport by minimizing their scattering

at GBs. However, grain growth is often quite difficult to control and poorly understood in Sb_2S_3 absorbers. Conventional solution and evaporation processes and post-annealing approaches usually do not lead to large-grained compact thin films.[1a,2b,7b] To date, the great efforts to boost the performance of Sb_2S_3 solar cells mainly focus on device structure optimization, orientation regulation, interface engineering, band tailoring, charge transport layer modification, etc.[6a,13] There are few works aiming to regulate the microstructure of Sb_2S_3 films to increase the grain size. Since the microstructure of thin films greatly depends on the initial nucleation and growth, it is important to be able to rationally design and control the nucleation and growth processes of Sb_2S_3.[14] However, because of the complexity of the reactions involved in solution- and vapor-based systems, mechanisms of nucleation and growth remain obscure right now.[11,15] For example, for solution-based deposition, the adsorption and reaction of ions at the solid–liquid interface involve random processes, causing great difficulty in controlling the nucleation and growth of films.[16] Engineering the grains and the GB network to fabricate large-grained Sb_2S_3 absorber films remains challenging.

The nucleation and growth of thin films are closely associated with the in situ chemical environment of precursors for deposition. Lanthanide ions have been successfully used to regulate the crystallization process and materials properties of semiconductors, such as $CsPbBr_3$ films and nanocrystals.[12a,17] Inspired by this fact, in this work, we investigated the incorporation of a variety of lanthanides (Ce^{3+}, La^{3+}, Gd^{3+}, Yb^{3+}, Er^{3+}, and Tm^{3+}) into the precursor solution for the hydrothermal deposition of Sb_2S_3 films, and found that the addition of Ce^{3+} allows effective grain engineering, which successfully resulted in large-grain Sb_2S_3 absorber films with ultralow-density GB networks. Systematic characterization was performed to clarify the role of Ce^{3+}, from which we propose that the formation of Ce_2S_3 at the CdS/Sb_2S_3 interface mediates nucleation and growth, leading to large-grained Sb_2S_3 films at the solid–liquid interface. As expected, this near-ideal microstructure of large-grain Sb_2S_3 films affords superior optoelectronic properties and significantly enhanced performance in planar heterojunction Sb_2S_3 solar cells. A competitive PCE of 7.66% was achieved, coupled with a record V_{OC} value of 796 mV for the Sb_2S_3 system. We performed a series of advanced measurements to understand in detail the effects of Ce^{3+} addition on nonradiative recombination in the Sb_2S_3 photovoltaic devices to rationalize the reasons behind the improvement in performance. This study therefore develops a novel method for tuning the grain size of Sb_2S_3 thin films to realize high-performance photovoltaic devices.

2. Results and Discussion

2.1. Preparation of Large-Grained Sb₂S₃ Thin Films

We employed the hydrothermal method to deposit Sb_2S_3 absorber films on $FTO/SnO_2/CdS$ substrates, in which $C_4H_4KO_7Sb·0.5H_2O$ and $Na_2S_2O_3·5H_2O$ were used as Sb and S sources, respectively. An extra amount of extrinsic Ce-based salts were intentionally incorporated into the precursor solution. **Figure 1**a shows top-down scanning electron microscopy (SEM) images of Sb_2S_3 thin films after 180 min of growth, prepared

**ADVANCED
SCIENCE NEWS**

www.advancedsciencenews.com

**ADVANCED
MATERIALS**

www.advmat.de
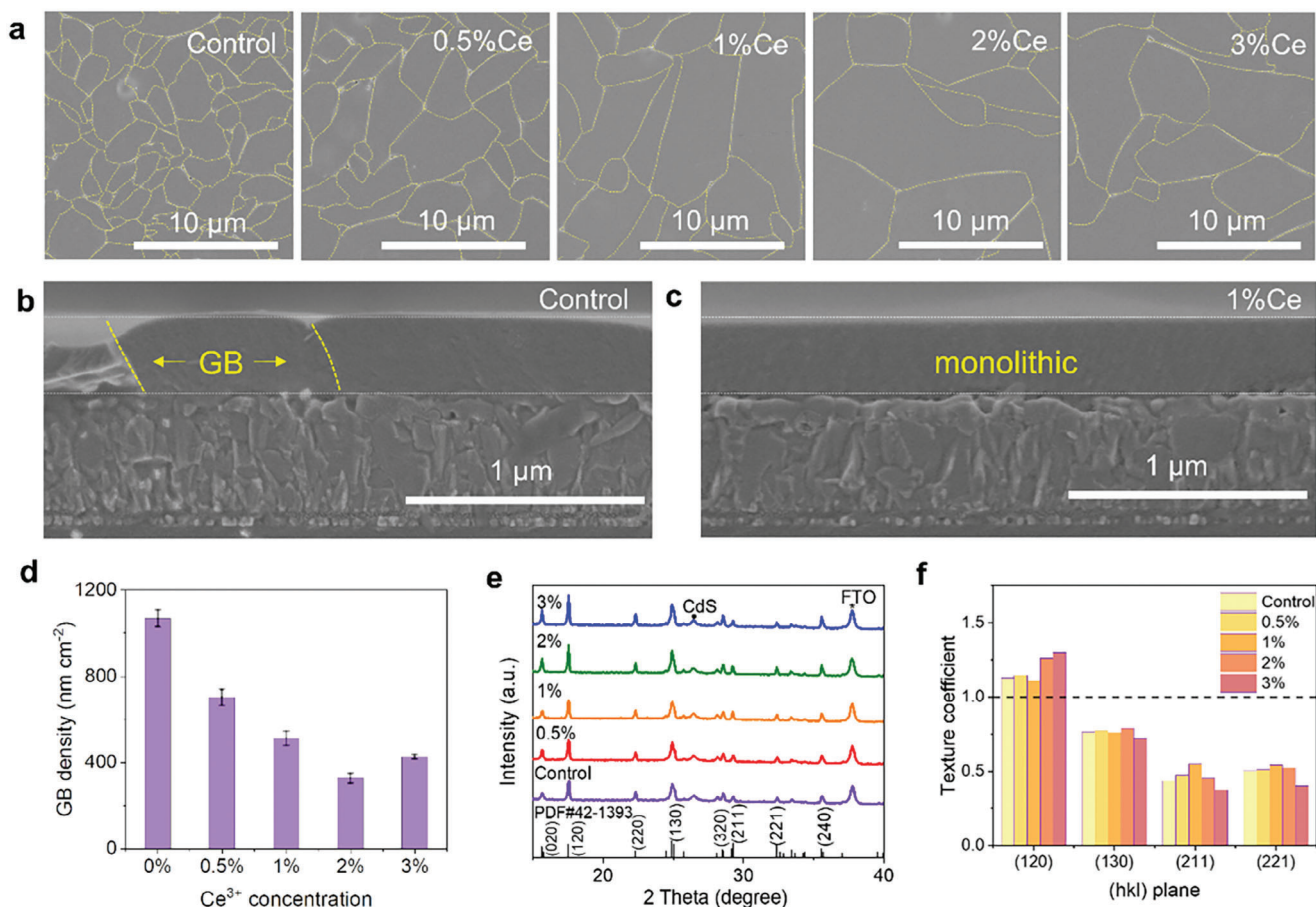
Figure 1. a) Top-view scanning electron microscopy (SEM) images of Sb_2S_3 thin films prepared without (i.e., control) and with the addition of $Ce(CH_3COO)_3$ salt, with molar ratios of Ce^{3+}/Sb^{3+} = 0.5%, 1%, 2%, and 3%. The hydrothermal deposition time was 180 min in all cases. The grain boundaries (GBs) are highlighted to show more clearly the changes in the GB density. b,c) Cross-sectional SEM images of the control Sb_2S_3 and 1%Ce-Sb_2S_3 films. d) The dependence of the GB density on the Ce^{3+} concentration in the precursor solution. Three samples were measured to determine the mean GB density values shown, and the error bars represent the standard deviation. e) X-ray diffraction (XRD) patterns of the control Sb_2S_3 film and Ce-Sb_2S_3 films prepared with different Ce^{3+} concentrations. f) Texture coefficients of the (120), (130), (211), and (221) peaks, which dominate the diffraction patterns of the Sb_2S_3 films.

without (i.e., control) and with the addition of different amounts of $Ce(CH_3COO)_3 \cdot xH_2O$. The molar ratio of Ce^{3+}/Sb^{3+} prepared in the precursor solution were 0.5%, 1%, 2% and 3%, and we hereinafter refer to the films prepared based on the ratios used in the precursor solution. As shown, the control Sb_2S_3 film has a grain size of 2.5-5.0 µm based on the characteristic diameters of grains, which is close to those reported in the literature.[11,15] The addition of Ce^{3+} into the precursor solution significantly increases the Sb_2S_3 grain size. When the Ce^{3+} concentration reaches 1%−3%, a large number of grains exceed 10 µm in size, with some grains even exceeding 15 µm. The cross-sectional SEM images of control Sb_2S_3 and 1%Ce-Sb_2S_3, as given in Figure 1b,c, reveal that as-obtained Sb_2S_3 grains span across the thickness of ≈280 nm absorber layers, which would facilitate efficient carrier transport between the charge transport layers.[10b] The addition of Ce^{3+} has negligible influence on the thickness of Sb_2S_3 layers; however, the control Sb_2S_3 film suffers from some vertical GBs while the 1%Ce-Sb_2S_3 sample affords monolithic grains. To further quantify the GB density, we defined it as the length of GBs per unit area, and calculated

the density of the GB network by first highlighting the GB grooves in top-down SEM images of Sb_2S_3 films. As shown in Figure 1d, the GB density on the Sb_2S_3 film surface is reduced from 1068 ± 40 nm µm^{-2} for the control sample to 702 ± 37, 511 ± 33, 327 ± 23, 427 ± 11 nm µm^{-2} for the 0.5%, 1%, 2%, and 3%Ce-Sb_2S_3 film samples, respectively. That is, the addition of Ce^{3+} into the precursor solution enables the well-controlled evolution of large grains with ultra-low GB density.

X-ray diffraction (XRD) patterns of Sb_2S_3 films without and with the addition of Ce^{3+} (Figure 1e) show the films prepared to be phase-pure, apart from peaks from the FTO substrate the films were deposited onto. The peaks from the absorber could all be indexed to orthorhombic Sb_2S_3 with a space group of *Pbnm* (JCPDS #42-1393).[1a,5] The dominant peaks are (120), (220), (130), (211) and (211). By calculating the texture coefficients of these peaks, we found that the addition of Ce^{3+} does not cause significant changes to the degree of preferred orientation (Figure 1f). In addition, the diffraction peaks show no evident shift with the addition of Ce^{3+}, which suggests that Ce^{3+} is not incorporated into lattice or interstitial sites.

**ADVANCED
SCIENCE NEWS**

www.advancedsciencenews.com

**ADVANCED
MATERIALS**

www.advmat.de
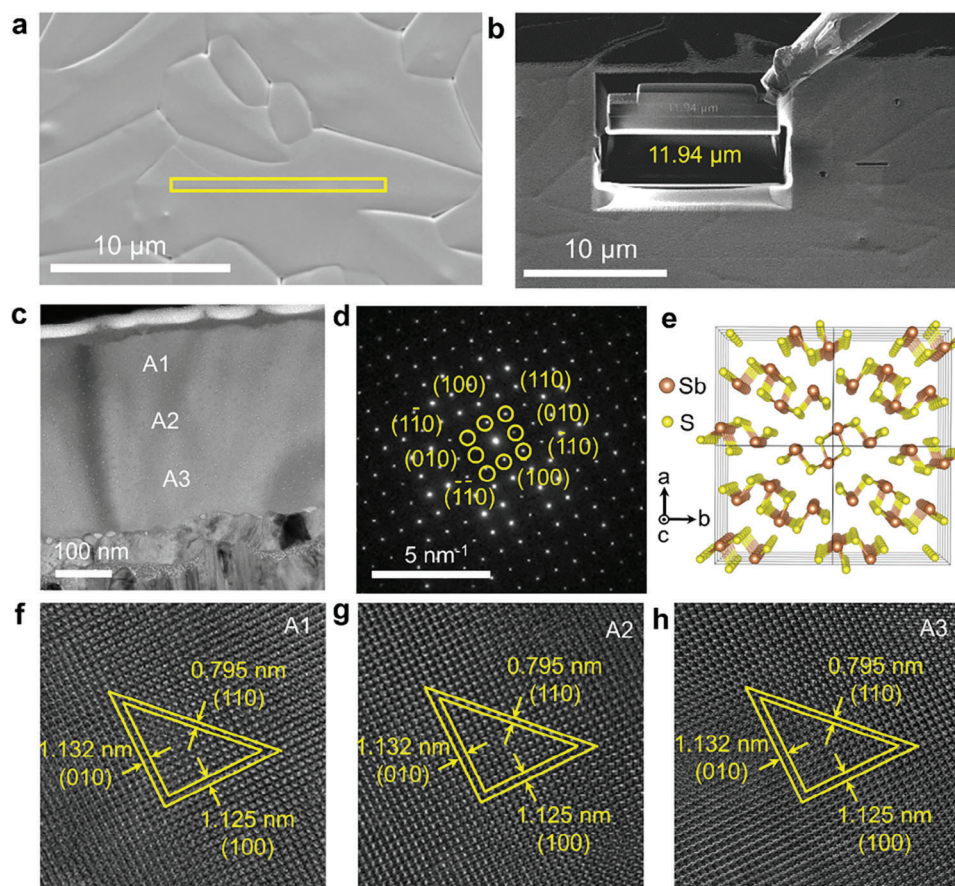
Figure 2. a,b) Scanning electron microscopy (SEM) images of the 1%Ce-Sb_2S_3 film used for making samples for transmission electron microscopy (TEM) characterization, and corresponding process of obtaining the lamella using a focused ion beam. c) Cross-sectional TEM image of 1%Ce-Sb_2S_3 sample deposited on FTO/SnO_2/CdS substrate. d) Selected area electron diffraction (SAED) pattern from Sb_2S_3 crystals, with diffraction spots indexed. e) Illustration of the crystal structure of Sb_2S_3, viewed from the [001] direction. f–h) High-resolution (HR) TEM measurements performed at points A1, A2, and A3 (see part c), and the corresponding lattice fringes.

By definition, a grain is the smallest microstructural unit that is a true single crystal and is bounded on all sides by GBs, interfaces, or surfaces.[14b] Since the microfeatures found from SEM images are not necessarily individual grains, we here further quantified this from transmission electron microscopy (TEM) measurements. **Figure 2**a,b shows SEM images of the 1%Ce-Sb_2S_3 film used for making samples for TEM characterization and corresponding process of obtaining the lamella using a focused ion beam (FIB) system, respectively. The cross-sectional TEM image (Figure 2c) reveals that the Sb_2S_3 film is compact and composed of large Sb_2S_3 grains spanning the thickness of the film. To verify whether the Sb_2S_3 grains are single crystalline, high-resolution TEM was used to analyze three arbitrarily selected points A1, A2, and A3 as labeled in Figure 2c, with the corresponding lattice fringes given in Figure 2f–h. As shown, lattice fringes with interplanar spacings of 1.132, 1.125, and 0.795 nm were identified, which corresponds to the (010), (100), and (110) planes in orthorhombic Sb_2S_3, respectively.[5] Points A1, A2, and A3 have identical crystallographic orientations, reflecting that the crystal planes extend from the top to the bottom of the Sb_2S_3 film. This confirms that the large grain is indeed single crystalline. The selected-area electron diffraction (SAED) pattern (Figure 2d),

which is observed from the [001] zone axis as illustrated by the atomic configuration of ribbon direction [001] orientation in the Sb_2S_3 crystal structure (Figure 2e), further confirms the single-crystalline nature of the Sb_2S_3 grains.

Atomic force microscopy (AFM) measurements (Figure S1, Supporting Information) further reveal that the 1%Ce-Sb_2S_3 sample displays much larger microfeatures than the control Sb_2S_3 sample. Moreover, the addition of Ce^{3+} results in a reduction in the average roughness of the absorber films from 13.1 nm (control) to 9.2 nm (1%Ce-Sb_2S_3). Flatter and more compact absorber films would enable the formation of high-quality P-N junctions. The conductive-atomic force microscopy (c-AFM) images and corresponding height profile and current analysis of the control Sb_2S_3 and 1%Ce-Sb_2S_3 films are provided in Figure S2a–d (Supporting Information). The intensity profiling of the surface current along the solid white line marked in Figure S2a−b (Supporting Information) reveals that the films suffer from evident current fluctuations at the GBs. The 1%Ce-Sb_2S_3 films have more homogeneous and slightly increased electrical conductivity across the 5 µm scale compared to the control film. The reduced fluctuation in the current intensity for 1%Ce-Sb_2S_3 films favors local photocurrent generation and collection,

**ADVANCED
SCIENCE NEWS**

www.advancedsciencenews.com

**ADVANCED
MATERIALS**

www.advmat.de

effectively suppressing carrier recombination at the GBs.[18] The Fermi level, valence band (VB) and conduction band (CB) of the control Sb_2S_3 and 1%Ce-Sb_2S_3 films can be derived from ultraviolet photoelectron spectroscopy (UPS) measurements (Figure S3a, Supporting Information; see details in Note S2, Supporting Information). A schematic diagram of the band positions of the functional layers in Sb_2S_3 solar cells is illustrated in Figure S3b (Supporting Information).[19] As shown, the Fermi level of the 1%Ce-Sb_2S_3 film is shifted up towards the CB compared to that of the control Sb_2S_3 film. The lower work function (WF) implies an increased electron carrier concentration, and therefore more n-type Sb_2S_3. We further performed Kelvin probe force microscopy (KPFM) measurements to map the surface potential of Sb_2S_3 films, as shown in Figure S2e–h (Supporting Information), which reveal a higher surface potential for the 1%Ce-Sb_2S_3 film in contrast to the control Sb_2S_3. An increased surface potential indicates a lower WF.[18,20] Therefore, the WF value of the 1%Ce-Sb_2S_3 sample would be lower than that of the control sample, implying the upshift of the Fermi levels as a result of increased background electron concentration.[21] To evaluate the conductivity of the absorber films, we measured the I–V curves in the dark based on a simple device configuration of FTO/Sb_2S_3/Au for the control Sb_2S_3 and 1%Ce-Sb_2S_3 film samples (Figure S4, Supporting Information). The 1%Ce-Sb_2S_3 film delivers an enhanced conductivity of 7.50×10^{-5} S cm^{-1}, higher than that of 4.32×10^{-5} S cm^{-1} for the control film, and this is consistent with the c-AFM results. Since the conductivity measurement here is out-of-plane and most of the GBs in Sb_2S_3 films are approximately vertical, the increase in conductivity σ reflects the increase of electron density according to the equation $\sigma = ne\mu_e$, where n is the electron concentration, e is the elementary charge, and μ_e is the electron mobility.

Finally, in addition to Ce^{3+}, we also investigated other lanthanide additives (La^{3+}, Gd^{3+}, Yb^{3+}, Er^{3+}, and Tm^{3+}). However, the addition of these ions into the precursor solution did not lead to the changes in microstructure obtained with Ce^{3+}, as shown by the SEM images and corresponding photovoltaic device performances given in Figure S5 and Table S1 (Supporting Information).

2.2. Growth Mechanism of Large-Grained Sb_2S_3 Films

To elucidate the underlying mechanism for the increase in Sb_2S_3 grain size, we performed control experiments as follows. Apart from using $Ce(CH_3COO)_3$ as the additive into the precursor solution, we investigated the use of Ce-based salts of $CeCl_3$ and $Ce(NO_3)_3 \cdot 6H_2O$, which were also found to be effective in promoting the grain size of Sb_2S_3 film, as reflected in the SEM images shown in Figure S6a,b (Supporting Information). In addition, we found that adding 1% molar ratio $Ce(CH_3COO)_3$ to the precursor solution for hydrothermal deposition would slightly increase the pH from 4.38 to 4.73. In order to exclude the influence of pH, we further used ammonia solution to adjust the pH of the precursor solution without the additive of Ce^{3+} to a similar level of 1% $Ce(CH_3COO)_3$ containing precursor, as summarized in Table S2 (Supporting Information). After examining the grain size of as-prepared Sb_2S_3 films with the addition of ammonia solution (Figure S6c, Supporting Information), we found that changing

pH has negligible influence on the grain size of Sb_2S_3. These results confirm that the increase in Sb_2S_3 grain size should be closely associated with the presence of Ce^{3+} in the precursor solution. In this work, we employed $Ce(CH_3COO)_3$ as the Ce-salt additive incorporated into the precursor solutions, unless otherwise stated.

Next, we clarified the specific effects of Ce^{3+} on the growth of Sb_2S_3 films and corresponding device performance. Generally, extrinsic Ce^{3+} ions could be incorporated into the crystal lattice of Sb_2S_3 (i.e., doping) or concentrate at GBs or interfaces. Aiming to determine the exact location of Ce^{3+}, we performed secondary ion mass spectrometry (SIMS) measurements to analyze the vertical distribution of various elements across the 1%Ce-Sb_2S_3 film. The SIMS intensity profiles of C, Au, Sb, Sn, S, Cd, and Ce in FTO/SnO_2/CdS/Sb_2S_3/Spiro-OMeTAD/Au are shown in **Figure 3**a. Herein, we used ^{110}Cd and ^{142}Ce isotopes to avoid interference from other ions on identifying these elements. It is revealed that Sb and S distribute uniformly across the absorber layer (t = 205–385 s). At the CdS/Sb_2S_3 heterojunction interface (t = 385 s), an abrupt increase in the Ce profile peak was clearly observed, suggesting the accumulation of Ce-based compounds at the CdS/Sb_2S_3 interface. We speculate that the Ce^{3+} incorporated probably reacted with S-species in the precursor solution to generate Ce_2S_3 compounds on top of the pristine CdS layer. Moreover, the symmetric distribution of the Ce peak also excludes the possible gradient doping of Ce^{3+} into Sb_2S_3. The 3D-SIMS mapping images of Sb, Cd, Ce, and S elements (Figure S7, Supporting Information) further reflect that the location of Ce element at the CdS/Sb_2S_3 interface.

Figure 3b presents the HRTEM image at the CdS/Sb_2S_3 interface of the 180 min-deposited 1%Ce-Sb_2S_3 thin film, which reveals there to be an ultrathin interlayer. This interlayer has lattice fringes with the interplanar spacing of ≈0.204 nm, corresponding to the (002) plane of orthorhombic Ce_2S_3 (space group Pnam). X-ray photoelectron spectroscopy (XPS) was also performed to confirm the formation of Ce_2S_3 at the CdS/Sb_2S_3 interface. Here, in order to successfully characterize the CdS/Sb_2S_3 interface, we fabricated ultrathin 1%Ce-Sb_2S_3 film samples prepared with 15 min- and 30 min of hydrothermal deposition. These film samples were not etched by Ar$^+$ sputtering because of the limited amount of cerium compounds on the film surface. As shown in Figure 3c, the binding energies (BEs) of 538.5 and 529.2 eV are assigned to the Sb $3d_{3/2}$ and Sb $3d_{5/2}$ core levels of Sb_2S_3, respectively, while the peaks centered at 539.7 and 530.4 eV are ascribed to Sb_2O_3, probably arising from the partial post-oxidation of the film surface in air.[22] The BEs of S $2p_{1/2}$ and S $2p_{3/2}$ for both film samples are 162.6 and 161.4 eV, respectively (Figure 3d).[23] Figure 3e shows characteristic peaks of high-resolution Ce 3d, which presents two pairs of spin-orbit signals. The peaks located at 904.2 and 885.5 eV can be attributed to Ce $3d_{3/2}$ and Ce $3d_{5/2}$ for the Ce^{3+} state in Ce_2S_3, respectively. The other pair of peaks at 900.5 and 882.4 eV is assigned to the satellite peak of Ce^{3+}. The results are consistent with those reported in the literature for Ce_2S_3, indicating the existence of Ce^{3+}.[24] Moreover, the reduced Ce peak intensity for the 30 min-deposited film compared to the 15 min-deposited film as well as the quantitative analysis of atomic ratios further implies the preferential formation of Ce_2S_3 prior to the deposition of Sb_2S_3 (Table S3, Supporting Information). High resolution XPS spectra and spectral

**ADVANCED
SCIENCE NEWS**

www.advancedsciencenews.com

**ADVANCED
MATERIALS**

www.advmat.de
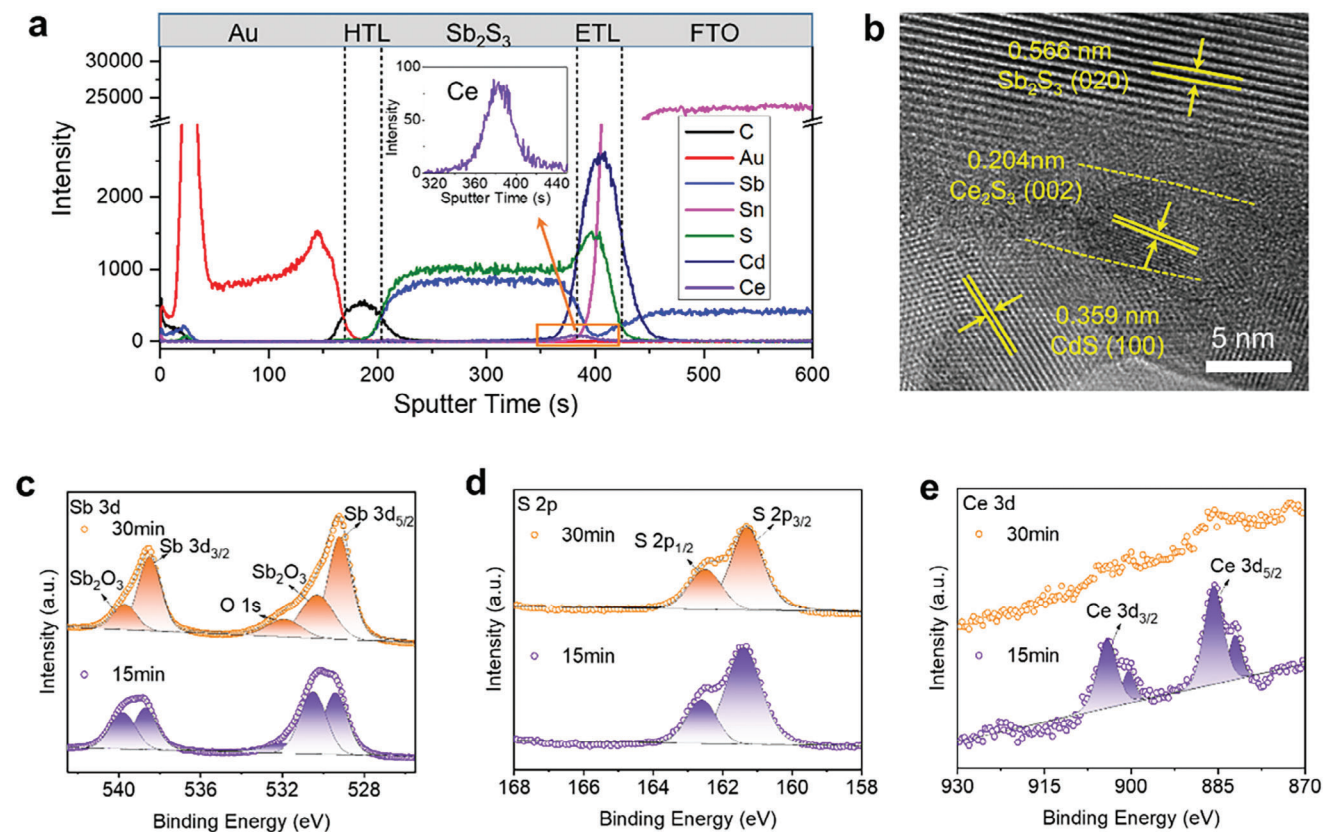
Figure 3. a) Secondary ion mass spectrometry (SIMS) depth profiles of the 180 min-deposited 1%Ce-Sb_2S_3 thin film. b) HRTEM image at the CdS/Sb_2S_3 interface of the 180 min-deposited 1%Ce-Sb_2S_3 thin film. c–e) High resolution X-ray photoelectron spectroscopy (XPS) spectra of Sb 3d, S 2p, and Ce 3d core levels, along with peaks fitted to these spectra, for the 15 min- and 30 min-deposited 1%Ce-Sb_2S_3 film samples.

deconvolution analysis of Sb 3d, S 2p, and Ce 3d for 180 min-deposited control Sb_2S_3 and 1%Ce-Sb_2S_3 film samples are given in Figure S8 (Supporting Information). The failure to detect the Ce 3d peak implies the absence of Ce elements at the surface of Sb_2S_3 and excludes the uniform doping or distribution of Ce in the bulk Sb_2S_3 film.

To gain more insights into the evolution of the morphology with Ce^{3+} incorporation, we performed SEM measurements at different time intervals during film growth. Figure S9 (Supporting Information) shows top-down and cross-sectional view SEM images of the control Sb_2S_3 and 1%Ce-Sb_2S_3 film samples prepared with different deposition durations (15, 30, 60, 120, and 180 min) by hydrothermal growth. A comparison of the morphology of the control and 1%Ce-Sb_2S_3 films prepared with identical deposition times reveals that the addition of Ce^{3+} results in an increase in the grain size of Sb_2S_3 over the course of the entire deposition process sampled. Moreover, it seems to be difficult to deposit Sb_2S_3 onto pristine CdS at the initial stage of hydrothermal deposition (0–30 min). In contrast, when Ce^{3+} was incorporated, an evident film morphology change occurs for the 30 min-deposited sample, probably resulting from the preferential deposition of Ce_2S_3. Another interesting phenomenon is that the addition of Ce^{3+} also reduces the amount of white precipitate particles on the surface of Sb_2S_3 films, which may be due to suppressed homogeneous nucleation that occurs in hydrothermal solutions.[16c] In addition to measuring the morphology by top-

down SEM, we also measured the cross-section of these samples, and found that there was no distinct difference in the thickness of the Sb_2S_3 absorbers without or with the addition of Ce^{3+} (Figure S9c,d, Supporting Information).

Taken together, the TEM, XRD, SIMS, and XPS results exclude the possibility of substitutional or interstitial doping of Ce^{3+} in the Sb_2S_3 host. Aiming to determine the complicated film growth route of hydrothermal deposition, it is worth noting that the overall reaction is a joint result of kinetic and thermodynamic processes. Although the Sb^{3+}, Ce^{3+}, and S^{2-} sources were simultaneously dissolved into the precursor solution, different ions have quite different release rates. S^{2-} ions are easily released from sodium thiosulphate ($Na_2S_2O_3$) upon hydrolytic decomposition. In contrast, considering the strong complexation effect of $[Sb_2(C_4H_2O_6)_2]^{2-}$, Sb^{3+} ions in the precursor solution involve quite slow ion release rates, especially at the very beginning of the reaction period. Generally, the deposition of Sb_2S_3 occurs when the ionic product (IP = $[Sb^{3+}]^2[S^{2-}]^3$) exceeds the solubility product of Sb_2S_3 (K_{sp} = $10^{-92.77}$).[25] Different from the complexation of $[Sb_2(C_4H_2O_6)_2]^{2-}$, the incorporated Ce-based salts can completely dissociate into free Ce^{3+} ions in the growth medium. That is, Ce^{3+} would be the dominating free cations available that could react with S^{2-} during the initial reaction stage, enabling the higher nucleation and deposition rate for Ce_2S_3. Meanwhile, Ce^{3+} is more active compared to Sb^{3+} reacting with S^{2-}, and thus the formation of Ce_2S_3 dominates the initial reactions during the
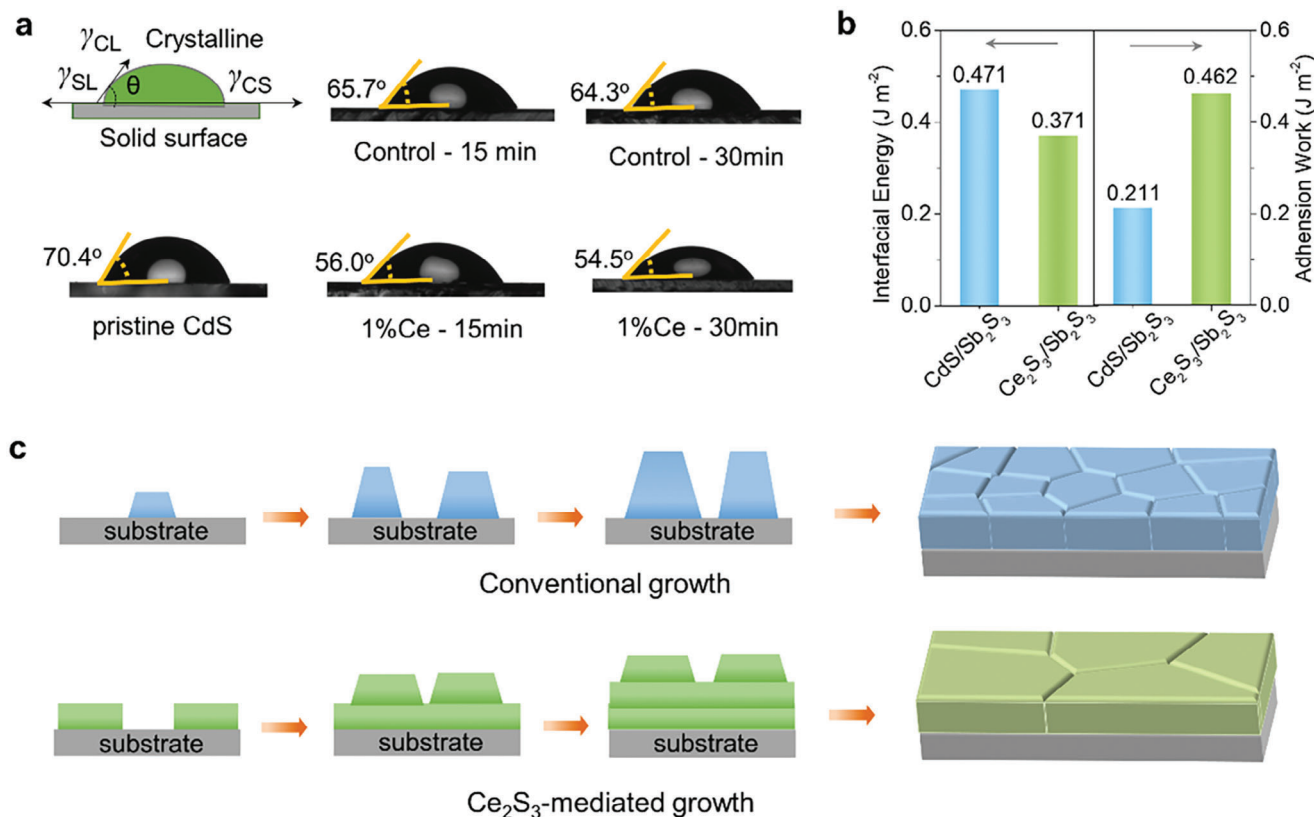
Figure 4. a) Illustration of the contact angle (θ) for heterogeneous nucleation, and the water contact angles of pristine CdS film, as well as CdS films that have undergone 15 min- and 30 min-hydrothermal deposition in Sb_2S_3 precursor solutions (both without and with 1% Ce). b) Histogram of the calculated interfacial adhesion work and interfacial energy for the heterointerfaces of CdS/Sb_2S_3 and Ce_2S_3/Sb_2S_3. c) Schematic illustrating conventional growth and Ce_2S_3-mediated growth of Sb_2S_3 thin films.

hydrothermal process. This can also be validated by the much lower formation energy of Ce_2S_3 (-1.99 eV atom^{-1}) compared to that of Sb_2S_3 (-0.27 eV atom^{-1}), as summarized in Table S4 (Supporting Information). Moreover, the limited supply of incorporated Ce^{3+} ions would only result in the formation of an ultrathin layer of Ce_2S_3 on top of the CdS layer, followed by a slow deposition of the Sb_2S_3 absorber layer. From the perspective of crystal growth, the deposition of Sb_2S_3 on the substrate is greatly influenced by the substrate characteristics, including chemical bonding environment and exposed crystal facets. We speculate that the pre-deposited Ce_2S_3 seeds succeed in modifying the initial nucleation environment of Sb_2S_3. Herein we can apply materials science principles of nucleation and growth to understand the microstructural evolution of Sb_2S_3 films and then propose a plausible mechanism.[14,26] The corresponding detailed descriptions of nucleation and growth are given in Note S1 (Supporting Information).

First, we measured the contact angle of water on the substrates used for Sb_2S_3 deposition to understand the specific role of the Ce_2S_3 interlayer on the nucleation behavior of Sb_2S_3. The interfacial energy diagram for two solids and a liquid in contact with each other is shown in **Figure 4**a, as well as the contact angle results of the pristine CdS film and the Sb_2S_3 films after 15 min- and 30 min- hydrothermal deposition with and without Ce^{3+}. Here γ_{CL}, γ_{SL}, and γ_{CS} denote the interfacial en-

ergies between the crystalline phase and the liquid, the substrate and the liquid, and the crystalline phase and the solid surface, respectively. As shown, the water contact angle of the pristine CdS film is as high as $70.4°$, which is slightly lowered to $65.7°$ and $64.3°$ for the films processed by 15 min- and 30 min-deposition without the use of Ce^{3+}, respectively. On the other hand, adding Ce^{3+} into the precursor solution dramatically reduces the water contact angle to $56°$ and $54.5°$ for 15 min- and 30 min-deposited samples, respectively. Since we have concluded that Ce_2S_3 seeds would be preferentially deposited via 15 min- and 30 min-hydrothermal deposition, it is evident that the substrate becomes more hydrophilic with the presence of an ultrathin Ce_2S_3 interlayer. Therefore, according to Equations (S1–S4) and Figure S10 (Supporting Information), during the nucleation stage, we suggest that the Ce_2S_3 interlayer promotes the heterogeneous nucleation of Sb_2S_3, while suppressing its homogeneous nucleation. This is because smaller contact angle results in a reduced energy barrier for heterogeneous nucleation. This scenario is similar to the case for perovskite films, which generally require a high density of heterogeneous nuclei on the substrate to afford uniform, full-coverage thin films.[27]

Subsequently, stable Sb_2S_3 nuclei will further grow to reduce the overall free energy of the system as long as the solute concentration is above the solubility limit. Typically, the growth of Sb_2S_3 films occurs by a process akin to the Volmer-Weber growth

2305841 (7 of 16)

model (island), where the interface energy is relatively large, and hence discrete nuclei form and grow before a layer is completed by infilling. Here the 3D nuclei (i.e., islands) first grow both vertically and laterally onto the CdS substrate, and then form a dense polycrystalline film.[14] For the case where a Ce_2S_3 interlayer is present, the growth of Sb_2S_3 films more closely resembles the Stranski–Krastanov model (layer plus island), where the interface energy is comparable to the island interaction energy, and hence layer formation competes with nuclei formation. Here, high-density small nuclei formed on the CdS/Ce_2S_3 substrate would tend more to grow laterally, which contrast to growth on the CdS substrate, and thus further coalesce into a large-grained Sb_2S_3 film. This hypothesis is further supported by first-principles calculations, which reveals decreased interfacial energy (γ) and increased adhesion work (W_{ad}) for the Ce_2S_3/Sb_2S_3 heterointerface compared to the CdS/Sb_2S_3 heterointerface. Interfacial energy and adhesion work are two important parameters to evaluate the properties of the heterointerface. The interfacial energy can be regarded as the resistance to form an interface structure; heterointerfaces with smaller γ are easier to form. Adhesion work, which is defined as the work required to separate two phases from each other (herein the film and the substrate), can be used to evaluate the bond strength of interfaces. Generally, a larger W_{ad} implies a stronger heterointerface stability. Here we built CdS/Sb_2S_3 and Ce_2S_3/Sb_2S_3 heterojunction models by selecting CdS (100), Sb_2S_3 (120), and Ce_2S_3 (001) surfaces as exposed surfaces. Table S5 (Supporting Information) gives the calculated surface energies of various crystal surfaces, and the calculated interfacial energy and adhesion work of two heterointerface are shown in Figure 4b. We can see that the interfacial energy of the Ce_2S_3/Sb_2S_3 heterointerface is 0.3705 J m^{-2}, lower than that of 0.4709 J m^{-2} for the CdS/Sb_2S_3 heterointerface. This suggests that the nucleation and growth of Sb_2S_3 on Ce_2S_3 is easier to occur. The reduced interfacial energy and enhanced bonding at the substrate/absorber interface might promote the transition of the growth mode of Sb_2S_3 from Volmer–Weber to Stranski–Krastanov , enabling the formation of large-grained Sb_2S_3 onto the substrate during the hydrothermal deposition process. The adhesion work of Ce_2S_3/Sb_2S_3 is 0.4616 J m^{-2}, larger than that of 0.2112 J m^{-2} for CdS/Sb_2S_3, which implies that the bond between Ce_2S_3 and Sb_2S_3 is stronger, resulting in the formation of a high-quality heterointerface with much more intimate contact.

Furthermore, the amorphous films will be transformed into compact and crystalline Sb_2S_3 films after annealing at a high temperature of 370 °C in this work. The Sb_2S_3 films would experience grain-coarsening during the postannealing treatment. According to the classical grain-coarsening mechanism, there is a thermodynamic driving force for favorable-oriented and/or large grains in a dense, polycrystalline thin film to increase in size. Note that the term "coarsening" here is used to imply a secondary grain-growth of an already-formed microstructure, as distinct from more general nuclei growth. Grain-coarsening often occurs in anisotropic films, where favorably-oriented grains involve rapid growth, giving rise to textured and large-grained films.[14a] In our case, all GBs in the Sb_2S_3 films intersect the top surface and the bottom interface with the substrate. The favorably-oriented grains refer to the ones whose low-energy crystal planes include the top surface and the interface with the substrate. The system tends to maximize the area of those surfaces and interfaces via the growth

of the favorably oriented grains at the expense of the less favorably oriented grains. The coarsening rate of those favorably oriented grains can be expressed by Equation (1):[14a]

$$\frac{dr_S}{dt} = M\left[\frac{(\gamma_S^* + \gamma_I^*) - (\gamma_S + \gamma_I) + \gamma_{GB}}{d}\right] \qquad (1)$$

where r_S is the radius of the secondary grain, M is the GB mobility; γ_S^* and γ_I^* are the average energies of the top surface of the film and the interface with the substrate, respectively, of all the normal grains; γ_S and γ_I are the surface and interface energies, respectively, of the favorably oriented grains; γ_{GB} is the GB energy; d is the film thickness. Equation (1) implies that, by minimizing the energy (γ_I) of the interface between the favorably oriented grains and the substrate through reasonable design of substrates for better adhesion, one can achieve rapid coarsening rate for grain-growth. Therefore, we suggest that the presence of Ce_2S_3 interlayer contributes to the better adhesion between Sb_2S_3 and the substrate, thus resulting in accelerated coarsening of favorably oriented Sb_2S_3 grains. The likely scenario for the evolution at the growth stage of conventional Sb_2S_3 films and Ce_2S_3-mediated Sb_2S_3 films is illustrated schematically in Figure 4c.

Based on these discussions, it is concluded that the significantly increased Sb_2S_3 grain sizes can be attributed to the Ce_2S_3 interlayer influencing the nucleation and growth of Sb_2S_3 deposited on top. The presence of the Ce_2S_3 interlayer could result in improved heterojunction quality with more intimate binding between the Sb_2S_3 layer and the substrate.

2.3. Device Performance of Sb_2S_3 Planar Solar Cells

Figure 5a schematically illustrates the typical planar superstrate device configuration (n-i-p) of $FTO/SnO_2/CdS/$ Sb_2S_3/Spiro-OMeTAD/Au, in which Sb_2S_3 is the absorber while SnO_2/CdS and Spiro-OMeTAD serve as the electron and hole transport layers, respectively. From the cross-sectional SEM images of the full device stack (Figure 5b), the Sb_2S_3 absorber layer is compact and uniform, with a thickness of 280 ± 10 nm. The photovoltaic parameters of such solar cells, each based on 20 devices, including V_{OC}, J_{SC}, FF, and PCE, obtained under AM 1.5G illumination (100 mW cm^{-2}), are given in the box charts of Figure 5c. The corresponding device photovoltaic parameters are summarized in **Table 1**. As shown, these devices exhibit good reproducibility and performance. With the addition of Ce^{3+} into the precursor solution, the PCE of Sb_2S_3 solar cells increased at first, before decreasing with further increases in Ce^{3+} concentration. The control Sb_2S_3 solar cells have an average PCE of 6.02%, whereas the average PCE was increased to 7.10% for the 1%Ce-Sb_2S_3 device. The current density-voltage ($J–V$) curves of the champion control Sb_2S_3 and Ce-Sb_2S_3 solar cells, are shown in Figure 5d. The control Sb_2S_3 solar cell has a V_{OC} of 772 mV, J_{SC} of 15.13 mA cm^{-2}, FF of 54.94%, and PCE of 6.42%. The best-performing 1%Ce-Sb_2S_3 device exhibits a PCE of 7.66%, coupled with a V_{OC} of 796 mV, J_{SC} of 16.67 mA cm^{-2}, and FF of 57.72%. That is, the addition of 1%Ce^{3+} leads to a relative PCE enhancement of 20% compared to the control device (or 1.24% absolute PCE increase). Figure 5f shows the evolution of the record PCE of Sb_2S_3 solar cells over the past few years, which reflects that this work demonstrates a competitive device efficiency at a comparable level to the
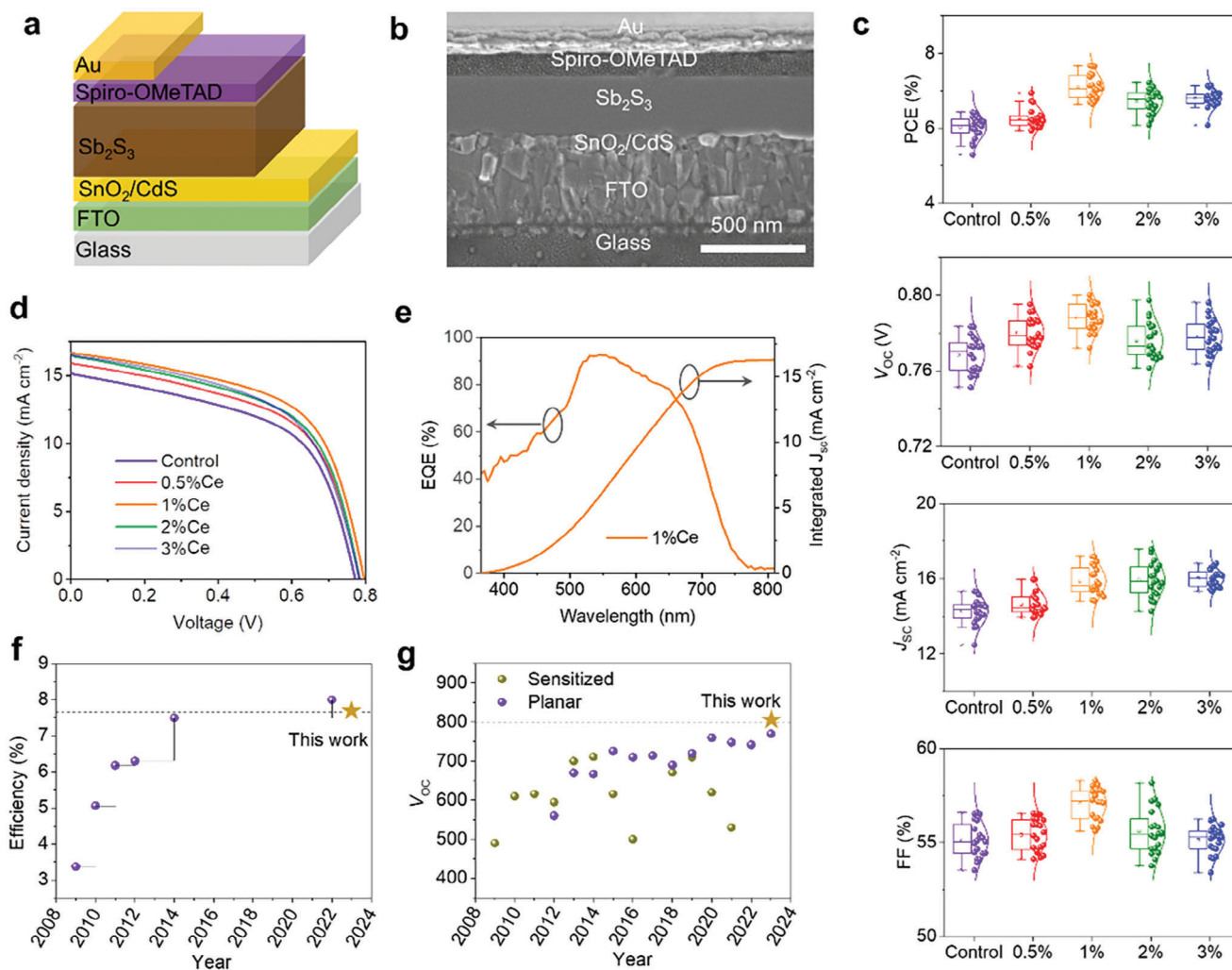
Figure 5. a) Illustration and b) cross-sectional scanning electron microscopy (SEM) image of the device structure, which have the configuration: $FTO/SnO_2/CdS/Sb_2S_3/Spiro-OMeTAD/Au$. c) The statistics of the performance parameters of the control Sb_2S_3 device and $Ce-Sb_2S_3$ devices obtained with the addition of different concentrations of Ce^{3+} to the precursor solution. A total of 20 devices were measured for each condition, and the performance metrics of each device is shown as individual data points. d) $J-V$ curves of the control Sb_2S_3 and $Ce-Sb_2S_3$ solar cells, measured under AM 1.5G (100 mW cm^{-2}) illumination. e) External quantum efficiency (EQE) curves of best-performing $1\%Ce-Sb_2S_3$ solar cells. f) Evolution in the record efficiency of Sb_2S_3 solar cells. g) V_{OC} values of previous work on well-developed planar and sensitized Sb_2S_3 solar cells.

Table 1. Average photovoltaic performance parameters of the control and $Ce-Sb_2S_3$ solar cells, measured under AM 1.5G illumination conditions.

Devices	V_{OC} [mV]	J_{SC} [mA cm^{-2}]	FF [%]	PCE [%]
Control	768 ± 9 (783)	14.26 ± 0.71 (15.33)	55.11 ± 0.93 (56.58)	6.02 ± 0.30 (6.42)
0.5%Ce	780 ± 8 (787)	14.67 ± 0.63 (15.97)	55.40 ± 0.85 (56.55)	6.27 ± 0.26 (6.94)
1%Ce	788 ± 7 (796)	15.91 ± 0.78 (17.19)	57.06 ± 0.84 (58.28)	7.10 ± 0.33 (7.66)
2%Ce	776 ± 10 (797)	15.99 ± 0.88 (17.57)	55.59 ± 1.17 (58.16)	6.72 ± 0.31 (7.21)
3%Ce	778 ± 9 (796)	15.99 ± 0.46 (16.82)	55.13 ± 0.74 (56.23)	6.79 ± 0.24 (7.13)

Format: mean ± standard deviation (best value).

recently-reported record efficiency of 8.00% for Sb_2S_3 solar cells. Figure 5e presents the external quantum efficiency (EQE) spectrum of the best-performing 1%Ce-Sb_2S_3 solar cells. The device shows a broad light response, ranging from 350 to 750 nm, with the peak EQE exceeding 85% in the visible wavelength range. The integrated J_{SC} from the EQE spectrum is 16.30 mA cm^{-2}, consistent with the J_{SC} measured from the $J–V$ curve (within 5% deviation). The EQE spectra of the other devices are given in Figure S11 (Supporting Information). As shown, the J_{SC} enhancement for Ce-Sb_2S_3 solar cells mainly comes from the long-wavelength range of 510–710 nm, indicating that the Ce-Sb_2S_3 devices afford more efficient charge transport and collection. Considering that the control Sb_2S_3 and Ce-Sb_2S_3 films have the same thicknesses, the enhancement in efficiency is attributed to more effective transport of charge-carriers in Ce-Sb_2S_3 than a higher density of charge-carriers being generated. Moreover, the Ce-Sb_2S_3 solar cells deliver improvements also in V_{OC} and FF. In particular, to the best of our knowledge, the V_{OC} obtained close to 800 mV is the highest value reported thus far for Sb_2S_3 solar cells. Figure 5g gives the V_{OC} values of well-developed planar and sensitized Sb_2S_3 solar cells (detailed in Table S6, Supporting Information). As shown, the trend in V_{OC} over the course of the development of Sb_2S_3 photovoltaics has recently stagnated at around 550–750 mV. This work therefore sets a new record of V_{OC} for Sb_2S_3 solar cells.

In addition to these improvements in the initial device efficiency, we found that Ce-Sb_2S_3 photovoltaics exhibited improved stability as well. We stored unencapsulated control Sb_2S_3 and 1%Ce-Sb_2S_3 devices in a cabinet with 15% relative humidity, and monitored the performance over time (Figure S12a, Supporting Information). The 1%Ce-Sb_2S_3 solar cell retained 97.1% of its initial efficiency after 30 days of storage, more stable in contrast to the control device that had 93.2% of the initial efficiency. Moreover, the unencapsulated devices also showed good stability under harsher damp-heat conditions (60% relative humidity, 50 °C). The control Sb_2S_3 and 1%Ce-Sb_2S_3 solar cells could retain 94.6% and 96.7% of their initial efficiencies, respectively, after 1-week of storage under these conditions (Figure S12b, Supporting Information).

It is worth noting that, increasing the Ce^{3+} concentration up to 5% and beyond resulted a sharp reduction in PCE (Figure S13a, Supporting Information). This phenomenon might be explained by the evolution in the morphology of Sb_2S_3 films. The Sb_2S_3 films appear to crack and peel off from the substrates, as reflected by SEM images of 5%Ce-Sb_2S_3 and 10%Ce-Sb_2S_3 films (Figure S13b,c, Supporting Information). This might have been caused by increased stress during the high-temperature annealing stage, causing cracking, delamination, and high roughness, similar to that reported for perovskite films.[28] Moreover, when Ce(NO$_3$)$_3$ and CeCl$_3$ were used to replace Ce(CH$_3$COO)$_3$ as the Ce^{3+} sources incorporated into the precursor solutions, the corresponding solar cells also delivered significantly enhanced performance (Figure S14, Supporting Information).

2.4. Defect Physics and Charge-Carrier Transport Properties

It is important to elucidate the defect characteristics of Sb_2S_3 films and further establish the relationship between defects and device performance. Deep-level transient spectroscopy (DLTS) was performed to explore the depth and quantity of defects in Sb_2S_3 films. As shown in **Figure 6**a, both the control Sb_2S_3 device and 1%Ce-Sb_2S_3 device present two negative DLTS signal peaks in the high temperature region due to the effect of multiple minority-carrier traps, i.e., hole defects in n-type Sb_2S_3 films.[1c] Each DLTS signal was fitted by using deep-level transient Fourier spectroscopy (DLTFS) and decomposed into two hole defects of different depths denoted as H1 and H2. The defect characteristics, including activation energy (E_a) and capture cross section (σ), and trap concentration (N_T) can be extracted from the linear fittings of the Arrhenius plots as given in Figure 6b, and the results are summarized in **Table 2**. The corresponding theory is given in Note S3 (Supporting Information). The E_a values of H1 and H2 are 0.45 and 0.77 eV, respectively. It is known that Sb_2S_3 consists of $[Sb_4S_6]_n$ chains which have five nonequivalent atomic sites, i.e., Sb1, Sb2, S1, S2, and S3. The quasi-1D crystal structure involves the presence of multiple defects in Sb_2S_3, including five vacancies (V_{Sb1}, V_{Sb2}, V_{S1}, V_{S2}, and V_{S3}), five anti-sites (S_{Sb1}, S_{Sb2}, Sb_{S1}, Sb_{S2}, and Sb_{S3}), and two interstitials (Sb_i and S_i), as predicted by previous theoretical calculations.[7a,b] By comparing the depth of defects obtained from measurements with the transition levels obtained from calculations, the H1 and H2 traps are consistent with two anti-site defects, S_{Sb1} and S_{Sb2}. It is revealed that both devices share identical types of deep-level defects; however, the concentrations of the H1 and H2 defects differ. Moreover, our hydrothermally deposited Sb_2S_3 films exhibit much lower defect density than Sb_2S_3 prepared by thermal evaporation.[29] The trapping capability of defects can be quantified by using the thermal trapping rate (C_{trap}), which is expressed by the equation $C_{trap} = 1/\tau_{trap} = \upsilon\sigma N_T$, where τ_{trap} is the carrier lifetime associated with the trap-assisted Shockley–Read–Hall (SRH) recombination and υ is the thermal velocity of charge related to the intrinsic charge transport feature of semiconductors. Therefore, minimizing defect density, particularly those with large capture cross sections, would increase minority carrier lifetimes and hence enhance V_{OC}. Here the impact of deep-level defects on the trapping of carriers of the control Sb_2S_3 device and 1%Ce-Sb_2S_3 device can be simply compared by the value of σN_T, as given by the statistical histogram of calculated σN_T for different hole traps (Figure 6c). It is revealed that H2 dominates charge trapping in absorber films in view of its larger σN_T value and greater energy depth. In contrast, the H1 defect would have limited carrier trapping capability because of its low capture cross section on the order of 10^{-18} cm^2, three orders of magnitude lower the 10^{-15} cm^2 value for the H2 defect. Hence, we assign H2 as the trap that is mainly responsible for the V_{OC} loss in the space charge region (SCR) of the solar cells. Compared to the control Sb_2S_3 device, the σN_T for the H2 defect in 1%Ce-Sb_2S_3 is decreased owing to a reduction in defect density. The band edge position and defect levels are illustrated in Figure 6d,e. Figure 6f gives the illustration of the defects of S_{Sb1} and S_{Sb2} in a $[Sb_4S_6]_n$ unit of Sb_2S_3 crystal structure. Since the depth of defects reflects the difficulty of charge emission from the traps, the H1 and H2 defects located at more than 0.3 eV above the VB would trap carriers without re-emission, thus acting as recombination centers and resulting in reductions in V_{OC}. These results suggest that the Ce-Sb_2S_3 films could decrease the defect density in absorber films and suppress charge-carrier recombination in solar cells.

ADVANCED
SCIENCE NEWS

www.advancedsciencenews.com

ADVANCED
MATERIALS

www.advmat.de
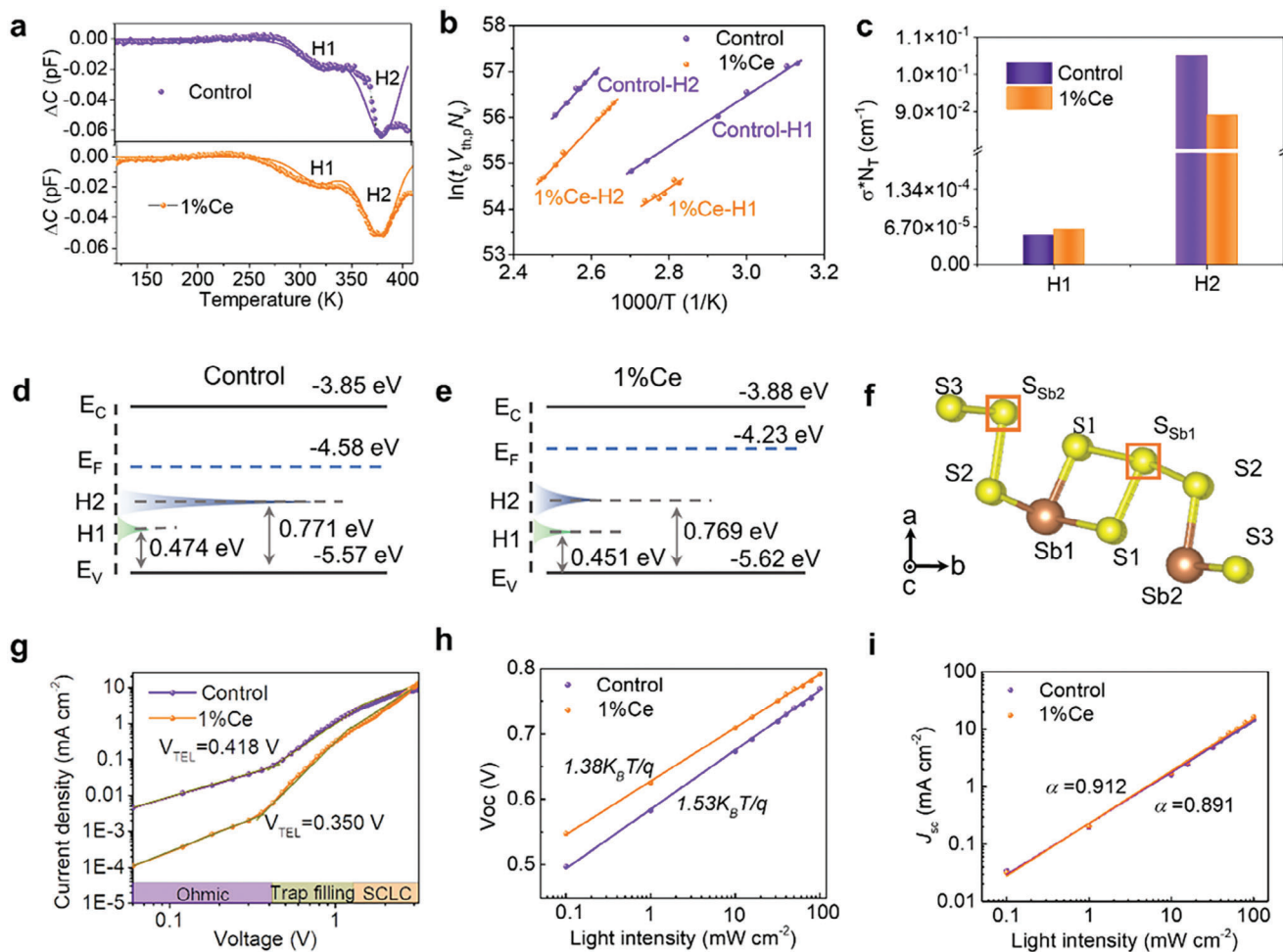
Figure 6. a) Deep-level transient spectroscopy (DLTS) signals from the control Sb_2S_3 and 1%Ce-Sb_2S_3 devices. b) Arrhenius plots derived from DLTS signals. The data points were obtained by calculating internal transients included in DLTS signals with the discrete Laplace transform, and the solid lines are corresponding linear fits. H1 and H2 correspond to S_{Sb1} and S_{Sb2} anti-site defects, respectively. c) The statistical histogram of calculated σN_T for different hole traps in the control Sb_2S_3 and 1%Ce-Sb_2S_3 devices. d,e) Schematic of band edge positions and defect levels of the control Sb_2S_3 and 1%Ce-Sb_2S_3, respectively, including CB (E_C) and VB (E_V) edges, Fermi level (E_F), and defect energy levels (H1, H2), relative to the vacuum level. f) Illustration of S_{Sb1} and S_{Sb2} defects in a $[Sb_4S_6]_n$ unit of Sb_2S_3 crystal structure. g) Space-charge limit current density (SCLC) measurements of the control Sb_2S_3 and 1%Ce-Sb_2S_3 based on the electron-only structure device of FTO/CdS/Sb_2S_3/PCBM/Au. h,i) The dependence of V_{OC} and J_{SC} on the light intensity for the control Sb_2S_3 and 1%Ce-Sb_2S_3 solar cells.

An increase in the band-tail states extending into the bandgap corresponds to an increase in the Urbach energy (E_U), which is a characteristic measure of the level of disorder.[30] As shown in the absorption spectra (Figure S15a, Supporting Information), the addition of Ce^{3+} decreases the band tailing of Sb_2S_3 films.

The bandgaps of control Sb_2S_3 and 1%Ce-Sb_2S_3 films were estimated to be 1.73 and 1.74 eV by using Tauc plots given in Figure S15b (Supporting Information). We used photothermal deflection spectroscopy (PDS), which is a highly sensitive technique to measure weak absorption at or below the bandgap, to

Table 2. Defect characteristics including the trap energy level (E_T), cross-section (σ), and trap concentration (N_T) in the control Sb_2S_3 and 1%Ce-Sb_2S_3 devices.

Devices	Trap	E_T [eV]	σ [cm²]	N_T [cm⁻³]	σN_T [cm⁻¹]
control Sb_2S_3	H1	E_V + 0.474	3.94×10^{-18}	1.33×10^{13}	5.24×10^{-5}
	H2	E_V + 0.771	2.32×10^{-15}	4.52×10^{13}	1.05×10^{-1}
1%Ce-Sb_2S_3	H1	E_V + 0.451	5.17×10^{-18}	1.22×10^{13}	6.30×10^{-5}
	H2	E_V + 0.769	6.85×10^{-15}	1.30×10^{13}	8.90×10^{-2}

**ADVANCED
SCIENCE NEWS**

www.advancedsciencenews.com

**ADVANCED
MATERIALS**

www.advmat.de

evaluate E_U. The Urbach energies of Sb_2S_3 and 1%Ce-Sb_2S_3 film samples were fitted to be 176 and 169 meV, respectively (Figure S15c,d, Supporting information). Although the obtained absolute E_U values might be overestimated due to the influence of the FTO/CdS substrate on the infrared absorption, which requires further study, the slight decrease in Urbach energy for 1%Ce-Sb_2S_3 is consistent in a decrease in sub-bandgap state density.

Space charge limited current (SCLC) measurements were conducted to evaluate the overall trap-state density of absorber films based on the electron-only devices FTO/CdS/Sb_2S_3/PCBM/Au. As shown in Figure 6g, at low bias voltage, the linear I–V curve suggests a typical Ohmic response. As the bias voltage increases and reaches the trap-filled limiting voltage (V_{TFL}), the curve presents a nonlinear feature because of the filling of injected carriers into trap-states.[23] The trap-state density can be estimated by using the equation $V_{TFL} = qn_\tau L^2/2\epsilon_r\epsilon_0$, where n_τ is the trap-state density, q is the elementary charge (1.60×10^{-19} C), ϵ_0 is the vacuum permittivity (8.85×10^{-12} F m^{-1}), ϵ_r is the relative permittivity of Sb_2S_3 (6.67), and L is the thickness of Sb_2S_3 film ($\approx$280 nm). The V_{TFL} values of the control Sb_2S_3 and 1%Ce-Sb_2S_3 devices are estimated to be 0.418 and 0.350 V, respectively. Hence the 1%Ce-Sb_2S_3 device involves reduced trap-state density (3.29×10^{15} cm^{-3}) compared to the control Sb_2S_3 device (3.94×10^{15} cm^{-3}). This reduction in the trap-state density is consistent with the result from DLTS characterization. The difference in the carrier concentrations obtained from DLTS and SCLC might be due to the fact that these two measurements were performed under different conditions. Firstly, I–V measurements from SCLC are steady state measurements, whereas DLTS involves transient measurements.[31] Secondly, the SCLC measurement is performed at room temperature to observe the total trap density, while the DLTS measurement was conducted from 120 to 410 K in this work. Thirdly, the sensitivity of SCLC and DLTS toward defects of different types and depths are also different. These factors may explain the different trap state densities derived from both techniques.

Light intensity-dependent J–V measurement is an effective strategy for assessing trap-assisted charge recombination loss mechanisms in solar cells. The dependences of V_{OC} and J_{SC} on the light intensity were conducted for the control Sb_2S_3 and 1%Ce-Sb_2S_3 solar cells. The corresponding semi-logarithmic plots, as shown in Figure 6h,i, can be achieved according to the relationship between V_{OC} (or J_{SC}) and light intensity as described by the relations $V_{OC} \propto (nK_BT/q)\ln(I)$ and $J_{SC} \propto I^\alpha$,[32] where I is the light intensity, K_B is the Boltzmann constant, T represents the absolute temperature, q is the elementary charge, and the values of n and α reflect the level of charge recombination. A diode ideality factor of unity occurs when recombination is entirely radiative, and a larger value implies more severe defect-assisted SRH recombination.[4a] The 1%Ce-Sb_2S_3 device delivers a smaller n of 1.38 than the control Sb_2S_3 device ($n = 1.53$), which is consistent with a reduction in nonradiative recombination. Moreover, as a result of the space charge effect, the value of α is often smaller than 1. Compared to the α value of 0.891 for the control device, the 1%Ce-Sb_2S_3 solar cell has a slightly larger α value of 0.912. However, these changes in α are too small to interpret. We further performed electrochemical impedance spectroscopy to investigate the charge transfer and recombination dynamics in solar cells.

Figure S16 (Supporting Information) shows the Nyquist plots of impedance spectra measured under dark, and corresponding fitting results based on the equivalent circuit model given in the inset are summarized in Table S7 (Supporting Information).[33] Clearly, the 1%Ce-Sb_2S_3 device shows an increased recombination resistance at the CdS/Sb_2S_3 interface ($R_{rec} = 16.80$ kΩ cm^{-2}) in contrast to the control device ($R_{rec} = 7.83$ kΩ cm^{-2}). A large recombination resistance would result in suppressed charge recombination and improved charge collection in photovoltaic devices.

We also carefully analyzed J–V curves of the control Sb_2S_3 and 1%Ce-Sb_2S_3 solar cells measured in the dark (Figure S17, Supporting Information), from which the parameters of junction ideality factor (A), the reverse saturation current density (J_0), the series resistance (R_s), and the shunt conductance (G, i.e., $1/R_{sh}$) can be extracted.[2a] The detailed description is provided in Note S4 (Supporting Information), and the overall fitting parameters are summarized in Table S8 (Supporting Information). The ideality factor plays a critical role to evaluate the junction quality as it reveals the main recombination mechanism of a p-n heterojunction. The calculated ideality factor of 1%Ce-Sb_2S_3 device ($A = 1.67$) is smaller than that of the control Sb_2S_3 device ($A = 2.07$), implying the effective suppression of charge-carrier recombination for the 1%Ce-Sb_2S_3 device. Moreover, the 1%Ce-Sb_2S_3 device obtains the lower J_0 (8.7×10^{-8} mA cm^{-2}), the smaller R_s (4.93 Ω cm^{-2}), and the smaller G (0.005 mS cm^{-2}) compared to the control Sb_2S_3 device ($J_0 = 1.5 \times 10^{-6}$ mA cm^{-2}, $R_s = 13.42$ Ω cm^{-2}, $G = 0.023$ mS cm^{-2}), indicating the enhancement in charge extraction capability. These results demonstrated the improved heterojunction quality for 1%Ce-Sb_2S_3 devices as a result of reduced shunt-current leakage, contributing to the improvement of device performance.[19]

Ultrafast transient absorption (TA) spectroscopy measurements were performed on the control Sb_2S_3 and 1%Ce-Sb_2S_3 films deposited onto FTO/SnO_2/CdS substrates without any hole extraction layer for this study to understand the charge-carrier kinetics further. As shown in **Figure 7**a,b, the TA spectra show pronounced ground state bleach (GSB) negative peaks and positive photoinduced absorption (PIA) peaks. Specifically, the GSB peaks at 460–510 and 610–680 nm can be assigned to the state filling of CdS films and the ground state absorption of Sb_2S_3 films, respectively; the typical PIA peak appearing at 520–620 nm can be attributed to the formation of sulfide radical (S$^-$) due to photoexcited holes localized on the S atom of Sb_2S_3 lattice.[1c,4a,29,34] The transient dynamics are retrieved from the pseudocolor pictures (Figure S18a,b, Supporting Information). The transient kinetic decay (scatter) monitored at 560 nm for the control Sb_2S_3 and 1%Ce-Sb_2S_3 films are given in Figure 7c,d, which are well fitted by a phenomenological biexponential equation (Note S5, Supporting Information), and the corresponding results are listed in Table S9 (Supporting Information).[2b] The PIA peak gradually decreases as a result of the decay of trapped holes, i.e., the S$^-$ species, which we here attribute to nonradiative carrier recombination in Sb_2S_3 films.[4a,35] As shown, the 1%Ce-Sb_2S_3 sample exhibits larger τ_{av} values (4.82 ns) that of the control Sb_2S_3 sample (4.02 ns). The prolonged lifetime in the 1%Ce-Sb_2S_3 sample suggests the suppression of the bulk and/or interfacial charge-carrier recombination, consistent with the results from DLTS characterizations. That is, the TA analysis reveals a slower charge

**ADVANCED
SCIENCE NEWS**

www.advancedsciencenews.com

**ADVANCED
MATERIALS**

www.advmat.de
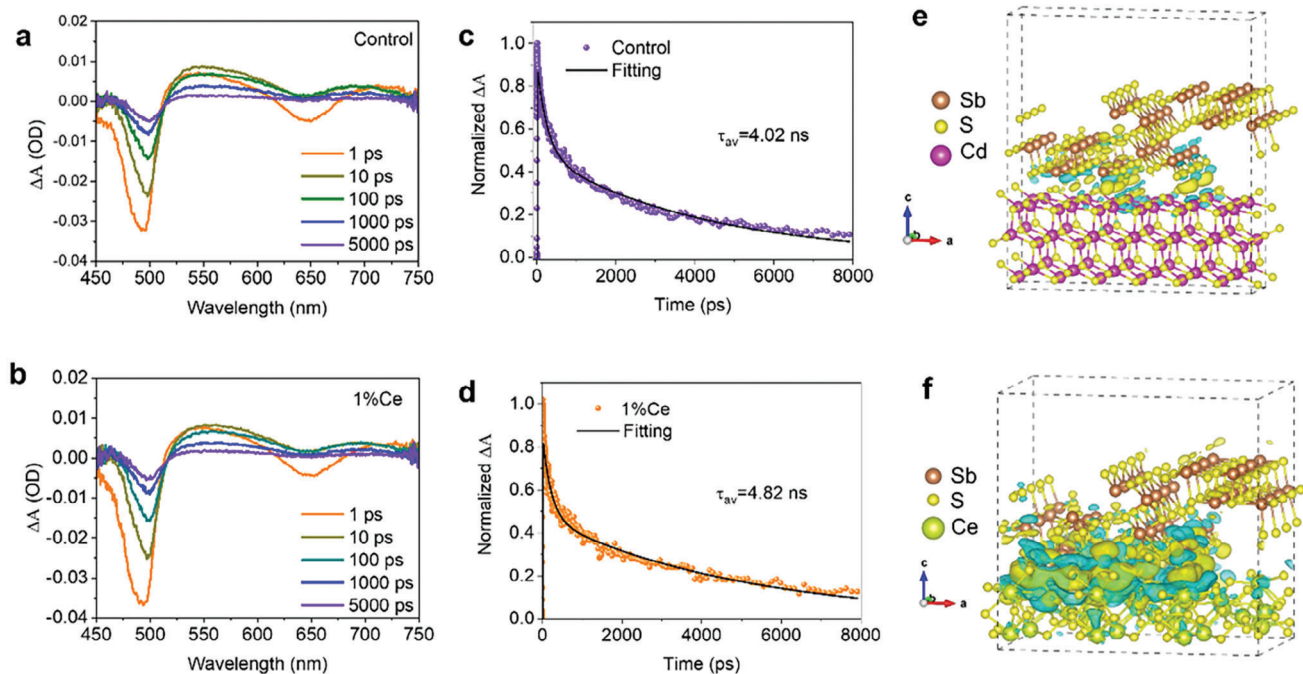
Figure 7. a,b) Transient absorption (TA) spectra obtained at 1, 10, 100, 1000, and 5000 ps pump-probe delay for control Sb_2S_3 and 1%Ce-Sb_2S_3 film samples. Excitation was with a 400 nm wavelength pulsed laser at a fluence of 251 μJ cm^{-2} pulse^{-1} and a repetition rate of 1000 Hz. c,d) Transient kinetic decay (scatter) and corresponding biexponential curve fittings (solid line) monitored at 560 nm of the control Sb_2S_3 and 1%Ce-Sb_2S_3 films. ΔA is defined as the change in the absorption of the sample before and after pumping. e,f) Diagram of the charge density difference analysis of the heterointerfaces of CdS/Sb_2S_3 and Ce_2S_3/Sb_2S_3.

recombination rate in 1%Ce-Sb_2S_3 films with larger grains. The prolonged lifetime of photoexcited minority hole carriers would eventually result in the improvement of V_{OC}.

Furthermore, we carried out charge density difference analysis to investigate the interaction at the heterointerfaces of CdS/Sb_2S_3 and Ce_2S_3/Sb_2S_3. As shown in Figure 7e,f, the yellow area means that there is charge accumulation there, while the blue area means that there is charge loss there. Due to the value of the isosurfaces in two models being identical, it is shown that, compared to the case of CdS/Sb_2S_3, the Ce_2S_3 surface has stronger charge transfer with the Sb_2S_3 surface. This calculation result corroborates the previous view that the bonding at Ce_2S_3/Sb_2S_3 heterointerface is stronger than that of the CdS/Sb_2S_3 heterointerface. That is, the presence of Ce_2S_3 contributes to the formation of a more ideal heterointerface, which would afford improved charge-carrier transport properties at the heterojunction in Sb_2S_3 solar cells.

3. Conclusion

In this work, we demonstrate a facile grain engineering strategy to deposit large-grained Sb_2S_3 films by adding Ce^{3+} into the precursor solution for hydrothermal deposition. Careful experimental characterization and first-principles calculations reveal that the incorporation of Ce^{3+} results in the generation of an ultrathin Ce_2S_3 interlayer at the CdS/Sb_2S_3 interface, which we propose promotes heterogeneous nucleation and horizontal growth of Sb_2S_3 grains due to a reduced free energy barrier for nucleation, as well as lower interfacial energy. The champion Sb_2S_3 solar

cell delivers a considerable PCE of 7.66%, superior to the control (6.42% PCE). High V_{OC}'s result, reaching values close to 800 mV, and is, to our knowledge at the time of publication, the new record for Sb_2S_3 solar cells. This enhanced performance might be attributed not only to suppressed charge-carrier recombination because of reduced detrimental defects at GBs and/or the CdS/Sb_2S_3 heterointerface, but also to improved charge-carrier transport across the heterojunction in Sb_2S_3 solar cells. Furthermore, although the large V_{OC} loss remains a bottleneck for the performance improvement of Sb_2S_3 solar cells, this work provides an important strategy that can be more broadly applied to increase the grain size and reduce the V_{OC} loss more generally in polycrystalline solar cells.

4. Experimental Section

Device Fabrication: Firstly, we fabricated SnO_2/CdS electron transport layers on fluorine-doped tin oxide (FTO, ≈15 Ω sq^{-1}) conductive glass substrates, which were thoroughly cleaned in advance by using detergent, deionized (DI) water, acetone, ethanol, and isopropanol, each for 20 min with ultrasonication and in sequence, followed by drying with nitrogen (N_2) airflow. The ultrathin SnO_2 layer was deposited by spin-coating commercial SnO_2 colloidal dispersion (15% in H_2O, Alfa Aesar) that was diluted seven times with DI water onto the conductive substrate at a speed of 3000 rpm for 30 s. Then as-prepared SnO_2 films were further annealed at 150 °C for 30 min. We used the CBD method to deposit CdS buffer layers. Typically, 30 mL of 15×10^{-3} M $Cd(NO_3)_2\cdot4H_2O$ (99%, Macklin) and 39 mL of ammonia solution in water (25%–28%, Sinopharm) were mixed together and stirred for 2 min. Then, 19.2 mL of 1.2 M thiourea (99.0%, Sinopharm) and 210 mL of DI water were further

2305841 (13 of 16)

**ADVANCED
SCIENCE NEWS**

www.advancedsciencenews.com

**ADVANCED
MATERIALS**

www.advmat.de

added, followed by another 2 min stirring. FTO/SnO$_2$ substrates were vertically immersed into such precursor solutions and maintained at 65 °C for 14 min with continuous stirring. Here, the thicknesses of SnO$_2$ and CdS layers in FTO/SnO$_2$/CdS substrates were about 10 and 60 nm, respectively, according to our previous work.[32b] Afterwards, as-prepared CdS layers were treated with CdCl$_2$ by spin-coating 0.088 M CdCl$_2$·2.5H$_2$O (99.0%, Sinopharm) in methanol solution onto CdS layers, followed by further annealing in air at 400 °C for 10 min. Secondly, the Sb$_2$S$_3$ absorber films were deposited onto FTO/SnO$_2$/CdS substrates by hydrothermal deposition, in which C$_4$H$_4$KO$_7$Sb·0.5H$_2$O (99.0%, Sinopharm) and Na$_2$S$_2$O$_3$·5H$_2$O (99.5%, Aladdin) were employed as Sb and S sources, respectively. A mixture solution with 20×10^{-3} M C$_4$H$_4$KO$_7$Sb·0.5H$_2$O and 80×10^{-3} M Na$_2$S$_2$O$_3$·5H$_2$O diluted in 40 mL DI water was added into a 50 mL Teflon tank, and FTO/SnO$_2$/CdS substrates were immersed into the mixture with the conducting side facing down inside the tank and tilted at an angle of ≈75° with respect to the horizontal plane. For the addition of lanthanide ions, particular lanthanide salts were used in this work.The type and the amount of salts were stated in corresponding parts of main text and supporting information. The Teflon tank was then sealed and kept at 135 °C for 180 min. When the reaction ended and the tank cooled down, the substrates were taken out, followed by rinsing with DI water and drying with N$_2$ flow. Then, as-deposited films were annealed at 370 °C for 10 min in a N$_2$ filled glovebox. Thirdly, the hole transport layer was deposited onto absorber films by spin-coating the precursor at a speed of 3000 rpm for 30 s, followed by annealing under 100 °C for 10 min on a hot plate. Here the hole transport layer precursor was prepared by mixing 36.6 mg spiro-OMeTAD (99.8%, Xi'an Polymer Light Technology Corp.), 14.5 μL tert-butylpyridine (TBP, 96%, Aladdin), and 9.5 μL 0.52 g mL^{-1} of lithium bis(trifluoromethylsyfonyl)imide salt (99.95%, Aladdin) dissolved in acetonitrile (99%, Aladdin) in 1 mL chlorobenzene (anhydrous, 99.8%, Sigma). Finally, superstrate Sb$_2$S$_3$ solar cells were completed by thermal evaporation of 80 nm Au as back electrodes.

Characterization: XRD characterization was performed on an X'Pert PRO MPD diffractometer with the Bragg Brentano geometry, and a Cu K_α X-ray source ($\lambda = 1.5406$ Å) was used. SEM images of film samples were collected on a JEOL field emission scanning electron microscope (JSM-6700F) equipped with EDS. The GB densities were obtained by depicting the GB grooves in SEM images of films using Adobe Photoshop software. AFM images were collected on a Bruker atomic force microscope (Dimension Icon); SCM-PIT probes were used in both the KPFM and c-AFM measurements, and the scanning area was 5×5 μm. The lattice structure was studied by TEM (Talos F200S), and the specimens were made by using an FIB technique with a microsampling system (Thermo Scientific Helios 5 CX). The element distribution of thin films was obtained by using SIMS (TOF-SIMS 5, ION-TOF GmbH), in which the sputtering source is O$_2^+$ with the energy of 1 keV and the area of 86×86 μm. Ultraviolet-visible absorption spectra were collected on a CARY 5000 Agilent spectrophotometer. The absorbance was obtained by using the equation $A = -\log_{10}(T)$, where A is the absorbance, and T is the transmittance. XPS was conducted on a Thermo Scientific K-Alpha spectrometer (Al K_α excitation, 1486.6 eV). UPS was performed on Thermo ESCALAB XI (He I excitation, 21.22 eV). J–V curves of solar cells were measured under the illumination of 1-sun (AM 1.5G, 100 mW cm^{-2}) by using an Newport Oriel Sol 3A Solar Simulator, combined with a Keithley 2400 digital source meter. The active area of devices was defined by a 0.06 cm^2 mask. EQE measurements were conducted on a QTest Station 1000 ADI system (Crowntech. Inc) under the DC mode, and the excitation source was a 300 W xenon lamp (CT-XE-300) which was split into specific wavelengths via a M24-S 1/4m monochromator. Impedance spectra were collected on a Zahner workstation (Zennium Pro.) with an applied voltage of 0.6 V and a scanning range of 1 Hz to 1 MHz under dark, and the spectra were fitted by using Z-view software. The DLTS characterization was performed on a Phystech FT-1230 HERA DLTS system with a laser excitation at the wavelength of 405 nm and the power of 10 mW. The capacitances were recorded by a Boonton 7200 Phystech capacitance meter (high frequency, 1 MHz). The device samples were placed in the liquid helium cryostat with a temperature scan ranging from 120 to 410 K at an interval of 2 K. The reverse bias, optical pulse width, and period width were −0.4 V, 100 ms, and 200 ms, respec-

tively. PDS was performed in a custom setup working in the transverse configuration. A tunable light source consisting of a grating monochromator coupled with a quartz-tungsten halogen lamp served as a pump, after modulating with a mechanical chopper inducing periodic temperature oscillations at the sample surface. A probe laser beam was passed parallel to the sample plane, with its path deviated by the temperature gradient in the heat-transfer liquid (3 M Fluorinert FC-72) surrounding the sample. The beam deflection amplitude was measured with a quadrant photodiode and demodulated with a lock-in amplifier (Stanford Research Systems SR830). The ultrafast TA properties of films were performed on a Helios Ultrafast pump-probe system, where a nondegenerate pump-probe configuration was used to probe the transient dynamics in the femtosecond to nanosecond time region (50 fs to 7 ns) under ambient conditions. The pump pulses of 400 nm was obtained by using a beta barium borate (BBO) crystal to double the 800 nm pulse generated on an optical parametric amplifier, and the white light continuum probe pulses was formed by 800 nm femtosecond with a 2 mm sapphire plate for the 400–800 nm wavelength range.

Calculations: All first-principles calculations were performed via density functional theory (DFT) by means of generalized gradient approximation (GGA) of Perdew–Burke–Ernzerhof (PBE), implemented by the Vienna Ab Initio Simulation Package (VASP).[36] The projected augmented wave (PAW) pseudopotentials were adopted with a cutoff energy of 450 eV in the whole calculation process.[37] The convergence criterion for the electronic self-consistent field loop was set to be 10^{-5} eV. The crystal structures, the surface structure, and the heterojunction structure were optimized until the residual force were below 0.03, 0.05, and 0.05 eV Å^{-1}, respectively. The Sb$_2$S$_3$ (120), CdS (100), and Ce$_2$S$_3$ (001) surfaces were used to simulate the exposed surfaces. The CdS (100) and Sb$_2$S$_3$ (120) surfaces were selected as exposed surfaces to form the CdS/Sb$_2$S$_3$ heterojunction based on XRD patterns, while Ce$_2$S$_3$ (001) was suggested to be the exposed surface to combine with Sb$_2$S$_3$ (120) by carefully examining the HRTEM image at the interface of CdS/Sb$_2$S$_3$. Moreover, the Ce$_2$S$_3$ (001) was a nonpolar surface similar to the exposed (100) surface of CdS, so that the quality of two heterojunctions could be compared more objectively. Furthermore, for the surface relaxation, a vacuum layer with a thickness of 15 Å was used and the bottom layers of atoms were bound to simulate the bulk phase. The Ce$_2$S$_3$/Sb$_2$S$_3$ heterointerface was generated with $1 \times 5 \times 1$ Sb$_2$S$_3$ surface and $3 \times 1 \times 1$ Ce$_2$S$_3$ surface supercells, with a vertical spacing about 2.4 Å and lattice parameters of $a = 24.025$ Å, $b = 15.386$ Å, $c = 23.000$ Å. The CdS/Sb$_2$S$_3$ heterointerface was generated with $1 \times 2 \times 1$ Sb$_2$S$_3$ surface and $6 \times 1 \times 1$ CdS surface supercells, with a vertical spacing about 2.4 Å and lattice parameters of $a = 25.492$ Å, $b = 7.281$ Å, $c = 28.000$ Å. The D3 Grimme dispersion correction was employed during the calculation of heterointerface formation energies.[38] The corresponding k-point spacing of all models was less than 0.3 Å^{-1}. Specifically, the Brillouin zone of Ce$_2$S$_3$ surface, CdS surface, Sb$_2$S$_3$ surface, Ce$_2$S$_3$/Sb$_2$S$_3$ heterojunction, and CdS/Sb$_2$S$_3$ heterojunction were sampled by $(4 \times 2 \times 1)$, $(6 \times 4 \times 1)$, $(1 \times 9 \times 1)$, $(1 \times 2 \times 1)$, and $(1 \times 3 \times 1)$ k-points mesh with Gamma point centered, respectively. The calculating formula and detailed processes for formation energy, surface energy, interface adhesive work, interfacial energy, and charge density difference analysis can be found in Note S6 (Supporting Information).

Statistical Analysis: All statistical analyses were performed using Origin 2019 (OriginLab Corp). The data from SEM, AFM, TEM, SIMS, XPS, UPS, UV–Vis, PDS, contact angles, J–V, EQE, EIS, and TA spectra shown in the paper are the original data without normalization. The data from XRD and TA kinetic decays were normalized to 1. The PCE data points of 1-week device stability tests were normalized to the PCEs measured before aging. Linear fittings were applied to UPS, V_{OC}, and J_{SC} versus light intensity, SCLC, and PDS plots. The data points of Arrhenius plots derived from DLTS signals were achieved by calculating internal transients included in DLTS signals with the discrete Laplace transform, and further processed with a linear fitting. Biexponential decay function was applied to TA kinetic decays to analyze the carrier dynamics. Quantitative data were expressed as the mean ± standard deviation. The statistical distribution for the PCE, V_{OC}, J_{SC}, and FF were obtained from 20 devices, and the lower whisker, lower box edge, middle line, upper box edge, and upper whisker

**ADVANCED
SCIENCE NEWS**

www.advancedsciencenews.com

**ADVANCED
MATERIALS**

www.advmat.de

refer to minimum, 25th percentile, median, 75th percentile, and maximum of the dataset, respectively.

Conflict of Interest

The authors declare no conflict of interest.

Data Availability Statement

The data that support the findings of this study are available from the Oxford University Research Archive, with the DOI: 10.5287/ora-gjqokbbde . http://dx.doi.org/10.5287/ora-gjqokbbde

[1] a) S. Wang, Y. Zhao, B. Che, C. Li, X. Chen, R. Tang, J. Gong, X. Wang, G. Chen, T. Chen, J. Li, X. Xiao, *Adv. Mater.* **2022**, *34*, 2206242; b) Z. Duan, X. Liang, Y. Feng, H. Ma, B. Liang, Y. Wang, S. Luo, S. Wang, R. E. I. Schropp, Y. Mai, Z. Li, *Adv. Mater.* **2022**, *34*, 2202969; c) R. Tang, X. Wang, W. Lian, J. Huang, Q. Wei, M. Huang, Y. Yin, C. Jiang, S. Yang, G. Xing, S. Chen, C. Zhu, X. Hao, M. A. Green, T. Chen, *Nat. Energy* **2020**, *5*, 587; d) Y. Zhao, S. Wang, C. Li, B. Che, X. Chen, H. Chen, R. Tang, X. Wang, G. Chen, T. Wang, J. Gong, T. Chen, X. Xiao, J. Li, *Energy Environ. Sci.* **2022**, *15*, 5118.

[2] a) Y. Qi, Y. Li, Q. Lin, *Appl. Phys. Lett.* **2022**, *120*, 221102; b) Y. Zhao, S. Wang, C. Jiang, C. Li, P. Xiao, R. Tang, J. Gong, G. Chen, T. Chen, J. Li, X. Xiao, *Adv. Energy Mater.* **2021**, *12*, 2103015.

[3] X. Chen, B. Che, Y. Zhao, S. Wang, H. Li, J. Gong, G. Chen, T. Chen, X. Xiao, J. Li, *Adv. Energy Mater.* **2023**, *2*, 2300391.

[4] a) S. Chen, M. Li, Y. Zhu, X. Cai, F. Xiao, T. Ma, J. Yang, G. Shen, A. Ke, Y. Lu, W. Liang, H.-Y. Hsu, C. Chen, J. Tang, H. Song, *Adv. Energy Mater.* **2022**, *12*, 2202897; b) V. Pecunia, L. G. Occhipinti, R. L. Z. Hoye, *Adv. Energy Mater.* **2021**, *11*, 2170005; c) Y. Peng, T. N. Huq, J. Mei, L. Portilla, R. A. Jagt, L. G. Occhipinti, J. L. Macmanus-Driscoll, R. L. Z. Hoye, V. Pecunia, *Adv. Energy Mater.* **2020**, *11*, 2002761.

[5] R. Kondrotas, C. Chen, J. Tang, *Joule* **2018**, *2*, 857.

[6] a) S. Hadke, M. Huang, C. Chen, Y. F. Tay, S. Chen, J. Tang, L. Wong, *Chem. Rev.* **2022**, *122*, 10170; b) C. Chen, J. Tang, *ACS Energy Lett.* **2020**, *5*, 2294.

[7] a) Z. Cai, C.-M. Dai, S. Chen, *Sol. RRL* **2020**, *4*, 1900503; b) L. Guo, B. Zhang, S. Li, Q. Zhang, M. Buettner, L. Li, X. Qian, F. Yan, *APL Mater.* **2019**, *7*, 041105; c) S. Li, S. Lu, Y. Lu, J. Xue, K. Li, C. Chen, J. Tang, *J. Mater. Chem. A* **2022**, *10*, 11625.

[8] Z. Yang, X. Wang, Y. Chen, Z. Zheng, Z. Chen, W. Xu, W. Liu, Y. Yang, J. Zhao, T. Chen, H. Zhu, *Nat. Commun.* **2019**, *10*, 4540.

[9] X. Wang, A. M. Ganose, S. R. Kavanagh, A. Walsh, *ACS Energy Lett.* **2022**, *7*, 2954.

[10] a) R. Fukuda, T. Nishimura, A. Yamada, *Prog. Photovoltaics* **2023**, *31*, 678; b) M. Hao, T. Duan, Z. Ma, M.-G. Ju, J. A. Bennett, T. Liu, P. Guo, Y. Zhou, *Adv. Mater.* **2023**, *35*, 2211155; c) N. Nicoara, R. Manaligod, P. Jackson, D. Hariskos, W. Witte, G. Sozzi, R. Menozzi, S. Sadewasser, *Nat. Commun.* **2019**, *10*, 3980; d) C. Wang, Y. Zhao, T. Ma, Y. An, R. He, J. Zhu, C. Chen, S. Ren, F. Fu, D. Zhao, X. Li, *Nat. Energy* **2022**, *7*, 744; e) R. Zhou, J. Xu, P. Luo, L. Hu, X. Pan, J. Xu, Y. Jiang, L. Wang, *Adv. Energy Mater.* **2021**, *11*, 2011923.

[11] X. Jin, Y. Fang, T. Salim, M. Feng, S. Hadke, S. W. Leow, T. C. Sum, L. H. Wong, *Adv. Funct. Mater.* **2020**, *30*, 2002887.

[12] a) J. Duan, Y. Zhao, X. Yang, Y. Wang, B. He, Q. Tang, *Adv. Energy Mater.* **2018**, *8*, 1802346; b) R. Liu, C. Dong, L. Zhu, J. Chen, J. Huang, W. Cao, X. Zhang, C. Ge, S. Yang, T. Chen, M. Wang, *Appl. Mater. Today* **2022**, *27*, 101487.

[13] a) P. Myagmarsereejid, M. Ingram, M. Batmunkh, Y. L. Zhong, *Small* **2021**, *17*, 2100241; b) U. A. Shah, S. Chen, G. M. G. Khalaf, Z. Jin, H. Song, *Adv. Funct. Mater.* **2021**, *31*, 2100265.

[14] a) W. A. Dunlap-Shohl, Y. Zhou, N. P. Padture, D. B. Mitzi, *Chem. Rev.* **2019**, *119*, 3193; b) M. Jung, S. G. Ji, G. Kim, S. I. Seok, *Chem. Soc. Rev.* **2011**, *2019*, 48.

[15] H. Deng, Y. Zeng, M. Ishaq, S. Yuan, H. Zhang, X. Yang, M. Hou, U. Farooq, J. Huang, K. Sun, R. Webster, H. Wu, Z. Chen, F. Yi, H. Song, X. Hao, J. Tang, *Adv. Funct. Mater.* **2019**, *29*, 1901720.

[16] a) J. Han, X. Pu, H. Zhou, Q. Cao, S. Wang, Z. He, B. Gao, T. Li, J. Zhao, X. Li, *ACS Appl. Mater. Interfaces* **2020**, *12*, 44297; b) R. Liu, Z. Shen, Z. Wan, L. Zhu, J. Chen, C. Dong, W. Chen, W. Cao, B. Chen, X. Yuan, B. Ding, S. Yang, T. Chen, X. Tian, C. Chen, M. Wang, *Commun. Phys.* **2021**, *4*, 177; c) J. Zheng, C. Liu, L. Zhang, Y. Chen, F. Bao, J. Liu, H. Zhu, K. Shen, Y. Mai, *Chem. Eng. J.* **2022**, *446*, 136474.

[17] G. Pan, X. Bai, D. Yang, X. Chen, P. Jing, S. Qu, L. Zhang, D. Zhou, J. Zhu, W. Xu, B. Dong, H. Song, *Nano Lett.* **2017**, *17*, 8005.

[18] S. Rijal, D.-B. Li, R. A. Awni, C. Xiao, S. S. Bista, M. K. Jamarkattel, M. J. Heben, C.-S. Jiang, M. Al-Jassim, Z. Song, Y. Yan, *Adv. Funct. Mater.* **2021**, *32*, 2110032.

[19] X. Mao, M. Bian, C. Wang, R. Zhou, L. Wan, Z. Zhang, J. Zhu, W. Chen, C. Shi, B. Xu, *ACS Appl. Energy Mater.* **2022**, *5*, 3022.

[20] X. Jiang, F. Wang, Q. Wei, H. Li, Y. Shang, W. Zhou, C. Wang, P. Cheng, Q. Chen, L. Chen, Z. Ning, *Nat. Commun.* **2020**, *11*, 1245.

[21] X. Wang, R. Tang, C. Jiang, W. Lian, H. Ju, G. Jiang, Z. Li, C. Zhu, T. Chen, *Adv. Energy Mater.* **2020**, *10*, 2002341.

**ADVANCED
SCIENCE NEWS**

www.advancedsciencenews.com

**ADVANCED
MATERIALS**

www.advmat.de

[22] R. Tang, X. Wang, C. Jiang, S. Li, W. Liu, H. Ju, S. Yang, C. Zhu, T. Chen, *ACS Appl. Mater. Interfaces* **2018**, *10*, 30314.

[23] H. Zhou, J. Han, X. Pu, X. Li, *J. Materiomics* **2021**, *7*, 1074.

[24] a) K. Hui, J. Fu, J. Liu, Y. Chen, X. Gao, T. Gao, Q. Wei, C. Li, H. Zhang, M. Tang, *Carbon Energy* **2021**, *3*, 709; b) F. Xu, K. Meng, S. Cao, C. Jiang, T. Chen, J. Xu, J. Yu, *ACS Catal.* **2021**, *12*, 164.

[25] H. Maghraoui-Meherzi, T. Ben Nasr, N. Kamoun, M. Dachraoui, *Phys. B* **2010**, *405*, 3101.

[26] H. Si, Q. Liao, Z. Kang, Y. Ou, J. Meng, Y. Liu, Z. Zhang, Y. Zhang, *Adv. Funct. Mater.* **2017**, *27*, 1701804.

[27] D. Bi, C. Yi, J. Luo, J.-D. Décoppet, F. Zhang, S. M. Zakeeruddin, X. Li, A. Hagfeldt, M. Grätzel, *Nat. Energy* **2016**, *1*, 16142.

[28] D. Liu, D. Luo, A. N. Iqbal, K. W. P. Orr, T. A. S. Doherty, Z.-H. Lu, S. D. Stranks, W. Zhang, *Nat. Mater.* **2021**, *20*, 1337.

[29] W. Lian, C. Jiang, Y. Yin, R. Tang, G. Li, L. Zhang, B. Che, T. Chen, *Nat. Commun.* **2021**, *12*, 3260.

[30] S. R. Rondiya, R. A. Jagt, J. L. Macmanus-Driscoll, A. Walsh, R. L. Z. Hoye, *Appl. Phys. Lett.* **2021**, *119*, 220501.

[31] A. Tsormpatzoglou, D. H. Tassis, C. A. Dimitriadis, L. Dózsa, N. G. Galkin, D. L. Goroshko, V. O. Polyarnyi, E. A. Chusovitin, *J. Appl. Phys.* **2006**, *100*, 074313.

[32] a) J. Zhou, X. Wei, J. Zhu, X. Yang, H. Niu, L. Wan, P. Jiang, J. Xu, R. Zhou, G. Cao, *Sci. China Mater.* **2020**, *63*, 1151; b) J. Zhou, R. Zhou, J. Zhu, P. Jiang, L. Wan, H. Niu, L. Hu, X. Yang, J. Xu, B. Xu, *Sol. RRL* **2021**, *5*, 2100494.

[33] a) P. P. Boix, G. Larramona, A. Jacob, B. Delatouche, I. Mora-Seró, J. Bisquert, *J. Phys. Chem. C* **2011**, *116*, 1579; b) A. Guerrero, J. Bisquert, G. Garcia-Belmonte, *Chem. Rev.* **2021**, *121*, 14430 c) J. Li, L. Xiong, X. Hu, J. Liang, C. Chen, F. Ye, J. Li, Y. Liu, W. Shao, T. Wang, C. Tao, G. Fang, *J. Energy Chem.* **2022**, *66*, 374.

[34] a) J. A. Christians, D. T. Leighton, P. V. Kamat, *Energy Environ. Sci.* **2014**, *7*, 1148; b) X. Gong, Q. Sun, S. Liu, P. Liao, Y. Shen, C. Grätzel, S. M. Zakeeruddin, M. Grätzel, M. Wang, *Nano Lett* **2018**, *18*, 3969.

[35] R. Tang, S. Chen, Z.-H. Zheng, Z.-H. Su, J.-T. Luo, P. Fan, X.-H. Zhang, J. Tang, G.-X. Liang, *Adv. Mater.* **2022**, *34*, 2109078.

[36] J. P. Perdew, K. Burke, M. Ernzerhof, *Phys. Rev. Lett.* **1996**, *77*, 3865.

[37] G. Kresse, J. Furthmüller, *Phys. Rev. B* **1996**, *54*, 11169.

[38] S. Grimme, *J. Comput. Chem.* **2004**, *25*, 1463.

2305841 (16 of 16)